Numerical Demultiplexing of Color Image Sensor Measurements via Non-linear Random Forest Modeling

by

Jason Deglint

A thesis
presented to the University of Waterloo
in fulfillment of the
thesis requirement for the degree of
Master of Applied Science
in
Systems Design Engineering

Waterloo, Ontario, Canada, 2016

This thesis consists of material all of which I authored or co-authored: see Statement of Contributions included in the thesis. This is a true copy of the thesis, including any required final revisions, as accepted by my examiners.

I understand that my thesis may be made electronically available to the public.

Statement of Contributions

There are two journal papers and one conference paper that make up the majority of this thesis. The parts of the thesis that have been co-authored are listed below. Furthermore, the contribution from each author is also presented.

The first paper has been accepted to Nature Scientific Reports Journal in June 2016 and is titled *Numerical Demultiplexing of Color Image Sensor Measurements via Non-linear Random Forest Modeling*. The majority of Section 2.2, Section 2.3, Chapter 3, and Chapter 4 are copied verbatim from this journal paper. Minor modification have been made to these sections and chapters to improve the flow of this thesis. For this journal paper Jason Deglint (J.D.), Farnoud Kazemzadeh (F.K.), and Alexander Wong (A.W.) conceived and designed the concept. J.D. and A.W. designed the numerical demultiplexer and F.K. designed the spectral characterization system. J.D. and F.K. performed the spectral characterization. J.D. and F.K. performed the experiments. J.D., F.K., and A.W. performed the data analysis. Finally, J.D., F.K., A.W., Daniel Cho (D.C.) and David A. Clausi (D.A.C.) contributed to the writing and editing of the paper.

The majority of Chapter 5 of this thesis is copied verbatim from the published paper *Photoplethysmographic imaging via spectrally demultiplexed erythema fluctuation analysis for remote heart rate monitoring*. This paper was published in February of 2016 in the SPIE Photonics West conference proceedings. Minor modification have been made to this paper to improve the flow of this thesis. J.D., Audrey G. Chung (A.G.C.), Brendan Chywl (B.C.) and Robert Amelard (R.A.) collected the data for this chapter. B.C. extracted the signal from the collected data. J.D. set up and trained the demultiplexer described in Chapter 4. A.G.C. set up the erythema fluctuation calculation. J.D., A.G.C, and B.C. processed the data to find the erythema fluctuation calculation from the digital demultiplexer. J.D., A.G.C., B.C., R.A., F.K., Xia Yu Wang (X.Y.W.), D.A.C. and A.W. contributed to the writing and editing of this chapter.

Finally, the majority of Chapter 6 of this thesis is an expanded work of the published journal publication *Numerical Spectral Demultiplexing Microscopy of Measurements from an Anatomical Specimen*. This paper was published in the Vision Letters Journal in October 2015 by the KWVIS Society. Minor modification have been made to this paper to improve the flow of this thesis. J.D., F.K., and A.W. conceived and designed the concept of the multispectral microscope using the Raspberry Pi. J.D. and F.K. performed the spectral characterization. J.D and F.K. performed the experiments and data collection. J.D., F.K., and A.W. performed the data analysis. Finally, J.D., F.K., A.W. and D.A.C. contributed to the writing and editing of the paper.

Abstract

Due to recent advancements in technology, consumer digital cameras are becoming cheaper and easier to use. These consumer digital cameras, with Bayer color filter arrays (CFAs), allow for simultaneous capture of the red, green and blue (RGB) channels. To achieve higher spectral resolution, multispectral imaging systems use methods such as filter wheels and tunable filters to capture data in a sequential manner. However, in order to capture transient phenomena, one would need to capture spectral information of a 2D scene in a simultaneous manner. Therefore, there has been an on-going trend towards creating a simultaneous multispectral imaging system that uses a conventional consumer digital camera with a Bayer CFA. Such a system allows for a effective imaging of transient or dynamic phenomena with a low-cost and compact system. Currently, the main method to accomplish this is known as Wiener estimation which uses statistical assumptions of the relationship between the incoming spectra and the RGB measurements. However, these assumptions limit the ability to accurately predict the incoming spectra. Therefore, we leverage a comprehensive framework based on numerical demultiplexing of sensor measurements via spectral characterization of the image sensor CFA and non-linear random forest modeling. To create this numerical demultiplexing system we create a forward model from the spectral sensitivity of the imaging system, which is accomplished with a monochrometer. This forward model is then used to create a mapping of 10,000 randomly generated spectra to their corresponding RGB values. This mapping acts as our training set for our non-linear inverse model which utilizes the random forest modeling framework. Having constructed the numerical demultiplexer, we test the performance against the state-of-the-art Wiener estimation for both quantitative and qualitative experiments. In the first set of experiments, we performed a quantitative performance assessment of the proposed framework within a controlled simulation environment. The second set of experiments, validated the observations made from the first set of controlled simulation experiments within a real-world setting. More specifically, we used an icon with different colors as well as a scene of different color flowers to perform quantitative analysis. In these experiments, we show that the proposed numerical demultiplexer outperforms the state-of-the art and is a more robust and reliable way to infer higher spectra from RGB measurements. Having validated the numerical demultiplexer, we use it for two applications which are photoplethysmogrpahic imaging and multispectral microscopy. For photoplethysmogrpahic imaging we found that decomposing the RGB camera measurements into narrow-band spectral information can noticeably improve the prediction of heart rate estimation. In addition, we used the numerical demultiplexer for both a bright-field multispectral microscope as well as a dark-field fluorescence multispectral microscope, which illustrates its potential as a low-cost, portable, point-of-care system.

Acknowledgements

There are a number of people who I would like to thank that made my M.A.Sc. possible. All the following people helped me get to where I am today.

First off, I would like to thank both Alexander Wong and David Clausi for co-supervising me. I am grateful to both of you for giving the opportunity to study at the University of Waterloo at the VIP Lab. I had a very positive learning experience during my time as a Masters Candidate.

I also want to thank Farnoud Kazemzadeh for sharing his knowledge with me and helping me with experiments. I also greatly appreciate you walking me work through some conceptual concepts regarding multispectral imaging.

Finally, I want to thank two important women in my life: my mom and my girlfriend. Thank you Jane Deglint for proofreading all my work for journals, conferences and course projects. Thank you also to Taylor Riemersma for your love and support during my masters. I greatly appreciate both of your encouragement.

Dedication

I dedicate this thesis to my mom.

Thank you so much for helping and encouraging me during my transition from full time work to going back to school to pursue an education. Thank you for giving me a place to live, making my meals, and feeding me treats with tea when I studied during my first two years of my undergrad. Finally, thank you for your participation in life.

Table of Contents

List of Tables

List of Figures

Chapter 1

Introduction

Due to the recent decrease in cost and accessibility of technology, our world is full of cameras. Every individual who owns a smart phone is carrying a camera in their pocket, ready to be used at any time. In addition, governments and businesses are using cameras for a wide range of applications from surveillance to security. Furthermore, cameras also have a huge application in research and science. The Hubble space telescope is a glorified camera that images other galaxies and other astronomical bodies. Microscopes are also fitted with cameras in order to observe microscopic phenomena. Cameras are revolutionizing the way we live.

Though the modern digital camera is having a major impact on our lives, it still has some fundamental limitations [1]. These limitations, for example, are realized when we want to image a scene in dark or bright conditions. In addition, these images are inherently noisy and warped due to the characteristics of the sensors and lenses which make up the camera system. While these limitations may not be an issue for everyday imaging, it has a large impact when using these cameras for scientific imaging.

Over the last 10 years there has been a new branch of imaging known as computational imaging [2]. It entails modeling the imaging system being used, and correcting the final image based on this model. For example, Algolux, a company in Toronto Canada, is reinventing image processors for next-generation cameras [3]. Lytro, in California, USA, is another company revolutionizing the way we think about cameras. Lytro has designed and built the world's first professional light field camera [4]. This allows users to adjust aperture and change the focal point after the image has been captured. By combining hardware knowledge with software post-processing, they are able to turn noisy and warped images into clean and crisp images. This holistic approach of combining the hardware and

software allows the entire system perform as a single unit.

One area of computational imaging that has barely been explored is determining the spectral content of a scene from a conventional camera. In this thesis we create a numerical demultiplexing system which uses computational imaging techniques to infer multispectral data from a conventional red, green and blue (RGB) digital camera. By characterizing each colour channel of the camera system in the wavelength domain we are able to build a mathematical model that mimics the hardware imaging process. Using machine learning software techniques we are then able to predict higher spectral content of a scene based on the RGB camera measurements. The main advantage of such a system is that it is able to capture multispectral data in a simultaneous manner opposed to traditional multispectral imaging techniques which require sequential capturing techniques.

Knowing the spectral signature of different locations in a 2D spatial image opens many possibilities since the light matter interaction is unique for different materials. One example where higher spectral content adds value is in determining the grade of different meat based on the spectral signature [5]. By looking at this signature one can determine whether the meat is of high or low grade since information on the quality of the meat is embedded in the spectral signature. Another application is remote imaging of agricultural crops to determine the health of the crop [6]. Finally, this method of computational imaging can also potentially be used in imaging pieces of art in order to learn more about the materials the artist used [7].

In this thesis we use specifically use the numerical demultiplxer for two applications: photoplethysmographic imaging and multispectral microscopy. In the first application, we show that decomposing the RGB camera measurements into narrow-band spectral information can improve the prediction of heart rate estimation. In the second application, we create a multispectral microscope for brightfield multispectral microscopy for botanical specimens as well as for bright-field and darkfield multispectral microscopy for anatomical specimens.

Chapter 2

Background

In this chapter we discuss the main differences between consumer digital cameras, sequential multispectral imaging systems and simultaneous multispectral imaging systems. We also introduce the Wiener estimation, which is the current state-of-the-art for simultaneous multispectral imaging.

2.1 Consumer Digital Cameras

The functionality of consumer digital cameras require three separate sections which are the lens body, the sensor, and the image signal processor (ISP). First, the incoming light is collected and focused onto the focal plane of the sensor by the lens body. Normally, a consumer digital camera will have multiple lenses to best collect and focus the light.

Having focused the light, a digital CCD or CMOS sensor is placed at the focal plane of the lens body. The purpose of the sensor is to convert the analog signal of photons into a discrete digital signal. A 2D pixel array digitizes the signal spatially, while the intensity of light hitting the sensor is digitized by performing quantization on the analog signal.

To collect colour data of the scene a series of red, green and blue (RGB) micro-filters are placed in front of the sensor, which create the Bayer filter array as seen in Figure 2.1. Each of these micro-filters only pass red, green or blue light onto the CMOS or CCD sensor to be quantized into a digital signal. The choice of the RGB Bayer filter is based on the functionality of the human eye since the human eye is twice as sensitive to green than to red and blue. Nearly all colors that our eye can detect and differentiate can be broken into the RGB primary colours. The Bayer filter is able to collect spectral data across a broad

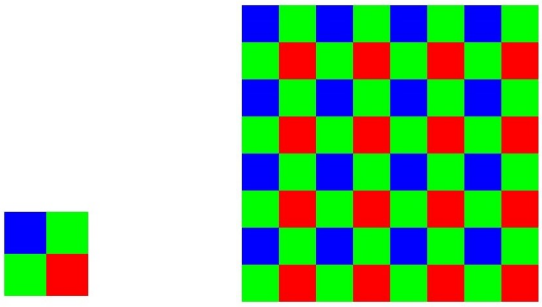

Figure 2.1: The Bayer colour filter array (CFA) is a repeat of a 2×2 base element. These filter only keep the red, green and blue (RGB) parts of the electromagnetic spectrum and use these three measurements to reconstruct a colour scene.

area of the visible part of the electromagnetic spectrum, effectively splitting the visible spectrum into three measurements.

Finally, these RGB measurements are passed into the image signal processor (ISP) for processing. For example, these measurements will usually undergo white-balance correction in order to achieve colour constancy, as well as JPEG compression for storage purposes.

The main advantage of a consumer digital camera is that in a single capture collects three course spectral measurements across the visible part of a 2D spatial scene. However, if more spectral bands with a higher spectral resolution would be needed, a consumer digital falls short.

2.2 Sequential Multispectral Imaging Systems

Multispectral imaging involves the capturing of imaging data of a particular scene or object at multiple wavelengths across a given part of the electromagnetic spectrum. Because different materials reflect, transmit, or emit at different wavelengths, multispectral imaging becomes a powerful tool to extract additional information about a scene or object. This approach facilitates unique material characterization and classification beyond what can be captured using conventional camera systems. As such, multispectral imaging has become a widely-used, powerful tool for different applications such as remote sensing [8, 9, 10], material analysis [11, 12, 13], and microscopy [14, 15, 16, 17].

Figure 2.2: A example of a filter wheel with seven optical bandpass filters for sequential multispectral imaging [18].

Traditionally, multispectral imaging has often been performed in a sequential manner, where imaging data are captured at a specific wavelength in the electromagnetic spectrum. Such sequential multispectral imaging systems typically consists of a monochromatic sensor and a spectral filtering mechanism such as filter wheels [19, 18], as seen in Figure 2.2, and tunable filters [20, 21] that allow the desired wavelength of light to pass through for acquisition. While highly useful for imaging static phenomena in a controlled environment, there are several limitations associated with such sequential multispectral imaging systems. First, such imaging systems require a complex optical setup involving many optoelectronic elements, leading to a more expensive and less compact system. Second, the temporal resolution of such systems is reduced because the imaging is done in a sequential manner. This reduction in temporal resolution makes imaging dynamic or transient phenomena more challenging.

The main advantage of multispectral imaging is that a high spectral resolution can be achieved. On the other hand, the disadvantage is that the data is normally captured in a sequential manner. Ideally, one would be able to capture high spectral information of a 2D scene in a simultaneous manner.

2.3 Simultaneous Multispectral Imaging Systems

To address such limitations, there has been an on-going trend towards simultaneous multispectral imaging systems, where the goal is to capture imaging data at all desired wavelengths at the same time. Such systems allow for effective imaging of dynamic or transient phenomena. The traditional implementation of such devices tend to be complex and costly since numerous beamsplitting optics as well as dedicated imaging devices are required, proportional to the desired number of spectral channels. There has been a recent surge in design and development of on-chip multispectral imagers that facilitate a less complex, and more compact design for simultaneous multispectral imaging. A major limitation of such systems revolves around the use of customized multispectral image sensors, where different sets of pixels in the sensor array are configured to capture imaging data at a particular wavelength. For example, Park *et al.* [22] propose a multispectral image sensor that is capable of capturing eight different wavelengths at the same time. However, such custom multispectral image sensors are complex to manufacture and cost-prohibitive for many real-world applications. As such, a method for simultaneous multispectral imaging that leverages off-the-shelf, low-cost image sensors with standard color filter arrays (CFAs) is preferred.

There has been recent interest in exploring simultaneous multispectral imaging systems where higher spectral resolution is obtained from off-the-shelf image sensors with CFAs [23, 24, 25, 26, 27, 28, 29]. Such an approach to simultaneous multispectral imaging is based on the notion that the general characteristics of reflectance spectra of the samples being imaged are typical and more constrained in diversity, which is true for a wide range of specific applications. In essence, one can better leverage the measurements from off-the-shelf image sensors with CFAs, given the inherent characteristics of the imaging sensor and the imaging process, to infer higher resolution reflectance spectra. While this approach is not as flexible and reliable as spectroscopic approaches for obtaining a very wide diversity of reflectance spectra, it has been demonstrated to be effective for a wide range of applications such as artwork assessment [23, 28], clinical skin imaging [25], vein visualization [30], hemodynamic visualization [31], and microscopy [16].

2.4 Wiener Estimation for Simultaneous Multispectral Imaging

The approach to use CFAs to obtain higher spectral resolution is highly appealing in suitable scenarios as it greatly decreases the complexity, size, cost, and increases the usability of multispectral imaging systems. In the most commonly-used configuration of this approach, simultaneous multispectral imaging, auto-correlation and cross-correlation are used to statistically model the relationship between the incoming light spectra and the image sensor measurements [23, 24, 25, 26, 27, 28]. The resulting auto-correlation and cross-correlation models are then used to infer higher resolution reflectance spectra from sensor measurements via Wiener estimation. These inherent statistical assumptions limit the ability to predict the complex spectra behaviors and as such may not scale well for obtaining fine structure in higher resolution spectra such as absorption or emission lines.

In general, inferring higher resolution spectra from CFA measurements requires a basic assumptions that the underlying spectra is smooth, positive, and bounded, which is true for most natural spectra [32]. Furthermore, since natural spectra have low effective dimensionality, many methods, such as the Wiener estimation, use a low-dimensional linear model to describe spectra [33]. We will also use the assumptions of positivity, smoothness, and boundedness when training our non-linear inverse model, however, the advantage over the Wiener estimation method is that we do not have to make any underlying statistical assumptions about the data, as seen in Chapter 3 and Chapter 4.

Chapter 3

Numerical Demultiplexing System

In this thesis we investigate the feasibility of performing simultaneous multispectral imaging of natural spectra using conventional sensors with Bayer CFAs. We leverage a comprehensive framework based on numerical demultiplexing of sensor measurements via spectral characterization of the image sensor and non-linear random forest modeling. By decoupling measurements that are captured using a low-cost, compact imaging system with conventional sensors with CFAs, one can then predict higher resolution spectral data across multiple wavelengths within the sensitivity of the image sensor.

The proposed numerical demultiplexing method can be summarized as follows. First, a comprehensive spectral characterization of the image sensor is performed. Second, given the spectral characterization information, a forward model is created that maps the input light spectra to the sensor measurements. Third, given the numerical forward model, the corresponding numerical demultiplexer is constructed via non-linear random forest modeling. This numerical demultiplexer can then be used to demultiplex simultaneously-acquired measurements made by the image sensor into reflectance intensities at discrete selectable wavelengths, resulting in a higher resolution reflectance spectrum. A more detailed description of each component of the proposed method is provided below.

In this study a Canon T3i APS-C CMOS image sensor was used to assess the feasibility of demultiplexing color image sensor measurements into higher spectral signals. The Canon T3i APS-C CMOS image sensor has a size of 22.3mm x 14.9mm and a Bayer pattern CFA, which we characterize in a comprehensive manner as described below.

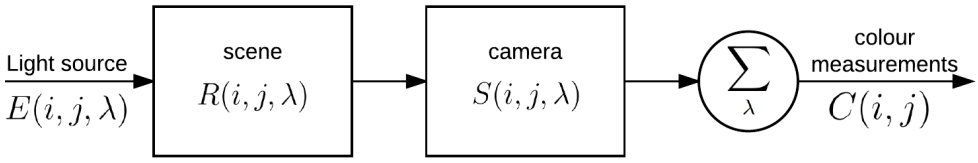

Figure 3.1: The intensity measurement on a sensor's pixel, $C(i,j)$, depends on the spectral sensitivity of the sensor $S(i,j,\lambda)$, the reflectance of the object $R(i,j,\lambda)$, and the light source $E(i,j,\lambda)$ which is used to illuminate the target.

3.1 Spectral characterization

To construct a numerical forward model characterizing the formation of image sensor measurements given input light spectra, we must first quantitatively characterize the inherent spectral sensitivity of the image sensor in a comprehensive manner. As seen in Figure 3.1, the intensity measurement on a sensor's pixel, $C(i,j)$, can be described as

$$C(i,j) = \sum_{\lambda} S(i,j,\lambda)R(i,j,\lambda)E(i,j,\lambda), \tag{3.1}$$

and depends on the spectral sensitivity of the sensor $S(i,j,\lambda)$, the reflectance of the object $R(i,j,\lambda)$, and the light source $E(i,j,\lambda)$ which is used to illuminate the target [34]. Here (i,j) is the pixel location on the sensor and λ is the wavelength at a given pixel. The spectral sensitivity, $S(i,j,\lambda)$, can be changed by placing a CFA over the sensor, which facilitates the simultaneous acquisition of multiple spectral bands: red, green, and blue in the case of a Bayer CFA.

We characterize the spectral sensitivity of a sensor for a given color in the CFA by emitting a large set of discrete narrowband light spanning the desired wavelength range onto the sensor, and then record the corresponding spectral response within the range of wavelengths. For example, a very common CFA used in consumer-level color imaging systems is the Bayer pattern CFA [35], which consists of red, green, and blue (RGB) filters placed on the sensor pixels resulting in three-channel spectral measurements. In this study, we designed and built a monochromator that enables wavelength selection in steps of 5 nm and we use the light emerging from the exit slit of the monochromator as an input into the camera to be imaged.

The focus of the camera is placed at infinity to ensure that the beam which impinges on the sensor is as close to collimation as possible, therefore uniformly illuminating a large

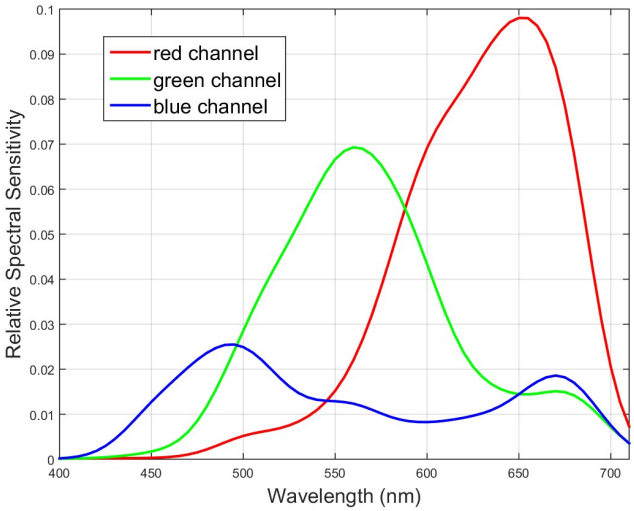

Figure 3.2: Spectral response of a Canon T3i APS-C CMOS image sensor with a Bayer pattern CFA. This spectral characterization is used to construct a forward model characterizing the formation of sensor measurements from light spectra hitting the sensor.

region on the sensor which results in a large number of each of the three color filters. Using this setup we characterize the spectral sensitivity of a Canon T3i APS-C CMOS image sensor with a Bayer pattern CFA using a set of 61 discrete test spectra ranging from 410 nm to 710 nm. The spectral response curve for the three filters are shown in Fig. 3.2.

3.2 Forward model

Given the spectral characterization of the color sensor, we can now construct a forward model characterizing the color measurement formation by the sensor with a CFA. As seem in Figure 3.3, by letting $\Lambda(i,j,\lambda) = R(i,j,\lambda)E(i,j,\lambda)$, Equation 3.1 can be rewritten as

$$C(i,j) = \sum_{\lambda} S(i,j)\Lambda(i,j,\lambda), \tag{3.2}$$

which can be written in matrix form as $\mathbf{C}_{p\times 1} = \mathbf{S}_{p\times n}\mathbf{\Lambda}_{n\times 1}$. Here $\mathbf{C} = [c_1 c_2 \dots c_p]^T$ represents the measurements made by the image sensor using the p filters in the CFA, $\mathbf{\Lambda} = [\lambda_1 \lambda_2 \dots \lambda_n]^T$ represents the intensities at n discrete selectable wavelengths of the

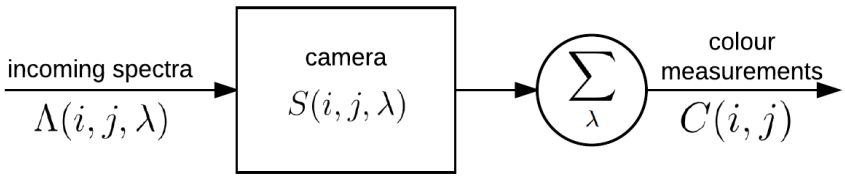

Figure 3.3: By letting $\Lambda(i,j,\lambda) = R(i,j,\lambda)E(i,j,\lambda)$, Equation 3.1 can be rewritten as Equation 3.2. This allows us to write the system in matrix form as $\mathsf{C}_{p\times 1} = \mathsf{S}_{p\times n}\mathsf{\Lambda}_{n\times 1}$.

light spectra arriving at the sensor, and S is the spectral sensitivity of the sensor. It is assumed that all pixels of a given filter have the same spectral response across the entire sensor. This relationship represents a forward model which maps the light spectra hitting the sensor to the sensor measurements made by the image sensor with a CFA.

3.3 Inverse model

At this stage, the goal is to construct a numerical demultiplexer based on the numerical forward model for the characterized image sensor described in Equation 3.2 and as seem in Figure 3.3. One can treat the numerical demultiplexer as an inverse problem of the numerical forward model, with the goal of determining higher resolution reflectance spectra $\mathsf{\Lambda}$ given the image sensor measurements C:

$$\mathsf{\Lambda} = \mathsf{S}^{-1}(\mathsf{C})\,. \tag{3.3}$$

Here $\mathsf{S}^{-1}(\cdot)$ is an inverse function that outputs the higher resolution reflectance spectra $\mathsf{\Lambda}$ given the sensor measurements C. Given the complex relationship between the higher resolution reflectance spectra and the sensor measurements, and the fact that we have an under-determined system in this case, one cannot obtain the inverse matrix $\mathsf{S}^{-1}(\cdot)$ analytically. Therefore, in the proposed framework, we propose that a numerical demultiplexer can be constructed through nonlinear modeling of the relationship between reflectance spectra and sensor measurements.

We leverage non-linear random forest modeling [36] to construct the numerical demultiplexer function $\mathsf{S}^{-1}(\cdot)$ using a comprehensive set consisting of 10,000 reflectance spectra and their corresponding sensor measurements based on the numerical forward model for the characterized image sensor. A random distribution of reflectance spectra was used

to construct the numerical demultiplexer to ensure that all wavelengths are well represented ensuring that the numerical demultiplexer achieves strong demultiplexing performance across the entire range of wavelengths. The nonlinear random forest model, used in this study for constructing the numerical demultiplexer, is comprised of 8,000 decision trees in total.

A key advantage of using such a non-linear random forest modeling approach to constructing the numerical demultiplexer is that it allows for reliable and flexible modeling of the complex relationships between reflectance spectra and sensor measurements without imposing strong assumptions about the nature of the relationship. Furthermore, we also introduce a numerical Wiener-based demultiplexer based on auto-correlation and cross-correlation models for comparison purposes with the proposed random forest-based demultiplexer. The Wiener-based demultiplexer based model is learned using the numerical forward model for the characterized image sensor described in Equation 3.2 by using the same comprehensive set consisting of 10,000 reflectance spectra and their corresponding sensor measurements based on the numerical forward model for the characterized image sensor.

Chapter 4

Demultiplexing RGB measurements to Multispectral Data

Given the constructed numerical demultiplexer in Chapter 3, one can now demultiplex simultaneously-acquired sensor measurements made by the characterized image sensor with a CFA into higher resolution reflectance spectra. In this chapter we performed three different sets of experiments to assess the feasibility of the proposed framework. For each set of experiments we discuss the experimental setup as well as the results. Finally, we discuss the outcome from all the experiments.

4.1 Methods Being Evaluated

The following three different methods will be tested to see their relative performance:

1. The state-of-the-art and popular Wiener Estimation (WEM) method [24, 25, 30], which was discussed in Section 2.4, and trained with the Macbeth chart [24].

2. The Wiener-based demultiplexer (DEMUX-WEM), which is same method in Section 2.4, but trained with the 10,000 spectra to RGB mappings created using the forward model in Section 3.2.

3. The random forest-based demultiplexer (DEMUX-RFM), where the inverse model used is an ensemble of decision trees as described in Section 3.3, and is trained with the 10,000 spectra to RGB mappings created using the forward model in Section 3.2.

The current state-of-the-art Wiener Estimation (WEM) method does not use a forward model but computes a statistic estimate of the incoming spectra based on the mapping of the spectra from the Macbeth chart to the RGB values [24]. Therefore, we use the forward model from of the imaging system from Section 3.2 to generate 10,000 spectra to RGB mappings and use this mapping to train a the Wiener-based demultiplexer (DEMUX-WEM) inverse model. Finally, due to the limitations of using the Wiener filter, as discussed in Section 2.4, we create a random forest-based demultiplexer (DEMUX-RFM) which allows for a non-linear inverse model. In the case of the DEMUX-WEM and the DEMUX-RFM the only priors are the generalized spectra, created from the mixed Gaussian model, and their mapping to RGB values created from the forward model. We base these generalized spectra on the assumption that the spectra will be positive, smooth, and bounded [32].

4.2 Experiment 1: Simulated Quantitative Assessment

In the first set of experiments, we wish to perform a comprehensive performance assessment of the proposed framework within a controlled simulation environment. The goal of this experiment is to determine the relative prediction accuracy of the three methods under evaluation.

4.2.1 Experimental Setup

A simulated sensor was constructed based on the characterization of the Canon T3i sensor with a Bayer pattern CFA, and a total of 10,000 new randomized simulated reflectance spectra were then generated and captured using the simulated sensor to generate sensor measurements. A random selection from the set of 10,000 test sensor measurements used in the first set of experiments is shown in Fig. 4.1. These RGB measurements were then fed into the numerical demultiplexer to obtain predicted reflectance spectra. The predicted reflectance spectra are then compared quantitatively against the original reflectance spectra entering the sensor using the peak signal-to-noise ratio (PSNR) to assess the fidelity of the demultiplexed spectra.

4.2.2 Results

The PSNR of WEM, DEMUX-WEM, and DEMUX-RFM for the first set of experiments were 14.7dB, 17.8dB and 20.16dB, respectively. The proposed DEMUX-WEM achieved

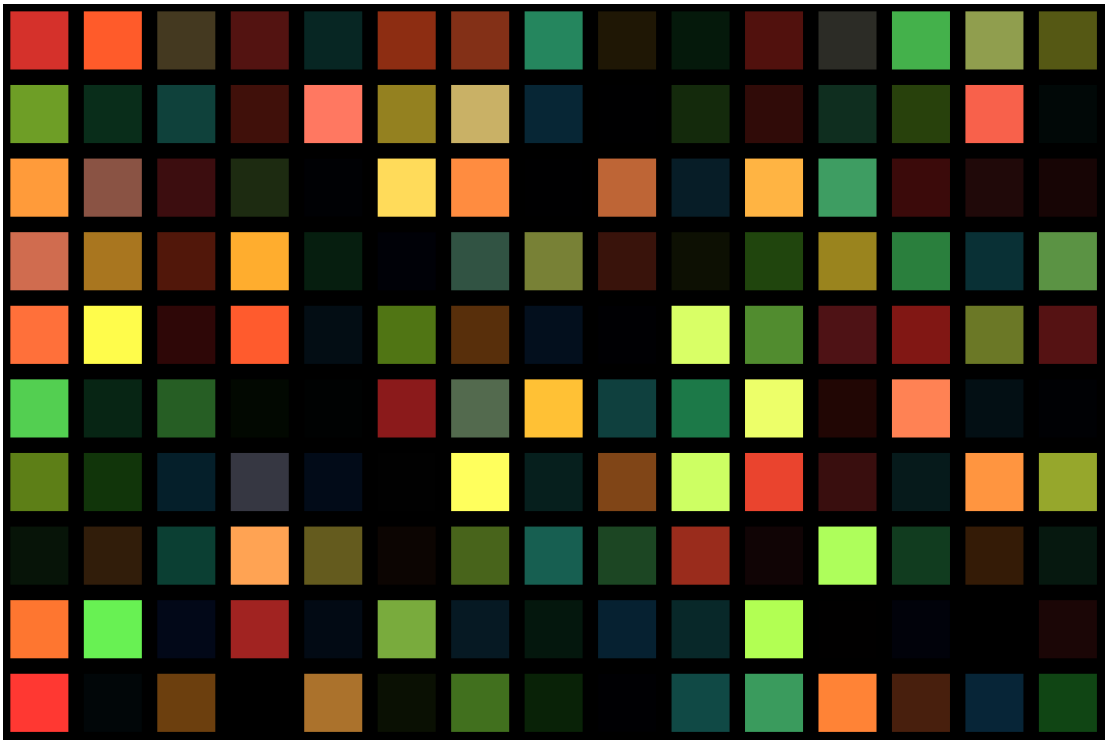

Figure 4.1: A random selection of 150 test sensor measurements (shown here as patches in a chart) from the set of 10000 test sensor measurements for Experiment 1.

a significant PSNR improvement over the traditional WEM, with the proposed DEMUX-RFM exhibiting significant PSNR improvements over the other two methods. This illustrates that the efficacy of the proposed DEMUX-WEM and DEMUX-RFM are providing more generalizable approaches for predicting a greater diversity of reflectance spectra. Three test reflectance spectra are shown in Fig. 4.2, along with the predicted spectra from the tested methods. The top two spectra exhibit the prediction accuracy with a unimodal shape while the bottom spectra exhibits the prediction accuracy with a bimodal shape. In all three cases, the proposed DEMUX-RFM provided the most accurate predicted spectra, followed by DEMUX-WEM and then WEM.

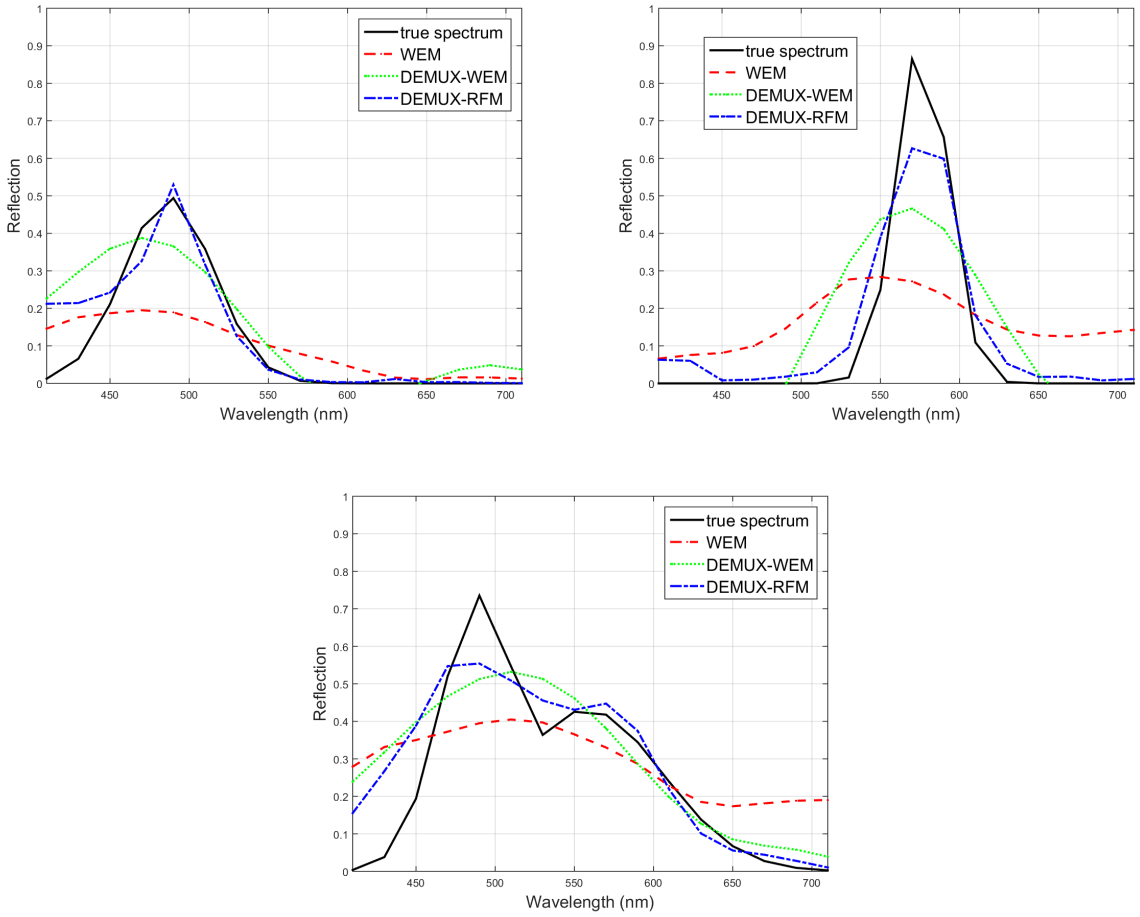

Figure 4.2: Three examples of simulated light spectra that were captured using the simulated sensor to obtain image sensor measurements (see Fig. 4.1). These sensor measurements were then used by the three tested approaches to predict higher resolution reflectance spectra. The proposed random forest-based demultiplexer (DEMUX-RFM) outperformed both Wiener estimation method (WEM) and proposed Wiener-based demultiplexer (DEMUX-WEM).

Figure 4.3: The test icon used in the second set of experiments. The true reflectance spectrum was measured for each unique section of the icon and then compared to the predicted spectra from the three inverse methods. These inverse methods are the state-of-the-art Wiener estimation method (WEM) and the proposed Wiener-based demultiplexer (DEMUX-WEM) and random forest-based demultiplexer (DEMUX-RFM).

4.3 Experiment 2: Real-world Quantitative Assessment

In the second set of experiments, we wish to validate the observations made from the first set of controlled simulation experiments within a real-world setting. We accomplish this by imaging an test target, with known spectral responses, and image this target with real camera. We then pass the RGB measurements into the three methods being evaluated and compare the results.

4.3.1 Experimental Setup

We used the real spectrally-characterized Canon T3i sensor with a Bayer pattern CFA to capture measurements of a test icon (see Fig. 4.3). The reflectance spectra of each section in the test icon was determined by measuring the sections using a high-resolution spectrometer while being illuminated by a Halogen-Tungsten (2650k) broadband light source under a 45° - 0° receiver-source setup. The true reflectance spectra were then found by detrending the measured spectra by the reflectance spectrum of the light source using a 99% reflectance target.

The sensor measurements were then fed into the numerical demultiplexer to obtain predicted reflectance spectra. The demultiplexed reflectance spectra from the numerical demultiplexer were then compared quantitatively against the known reflectance spectra of the icon using PSNR to assess the fidelity of the demutiplexed spectra.

4.3.2 Results

The PSNR of WEM, DEMUX-WEM, and DEMUX-RFM for the second set of experiments involving the test icon are 17.7dB, 13.3dB, and 17.2dB, respectively. While WEM achieves the highest PSNR in this set of experiments, it is important to note that the primary reason why WEM is able to achieve this level of performance is that the true reflectance spectra of the sections in the test icon very closely resembles the spectra of color patches in the Macbeth chart, which are used to train WEM as per [24]. Nevertheless, it is very interesting to observe that the proposed DEMUX-RFM, which is constructed based on the forward model of the characterized sensor, is able to achieve a PSNR that is very close to the WEM PSNR, with a difference of just 0.5dB, which illustrates the strength of the proposed framework.

The true spectra and predicted spectra from the test methods for the 'blue' and 'green' sections of the test icon are shown in Fig. 4.4. When predicting the spectrum of the 'blue' section, all three methods exhibited similar performance. However, when predicting the spectrum of the 'green' section, WEM and DEMUX-WEM exhibited similar performance while DEMUX-RFM achieved a more accurate prediction.

4.4 Experiment 3: Qualitative Assessment

In the final set of experiments, we wish to validate the observations made regarding the proposed framework in the first and second set of controlled simulation experiments within a real-world environment. To accomplish this, we used the real Canon T3i sensor with a Bayer pattern CFA to capture measurements a scene consisting of flowers of different colors.

4.4.1 Experimental Setup

We use the real spectrally-characterized Canon T3i sensor with a Bayer pattern CFA to capture measurements of a scene consisting of flowers of different colors to qualitatively illustrate the feasibility of the proposed framework (see Fig. 4.5). The sensor measurements were then fed into the three methods being evaluated to construct predicted reflectance spectra images at different spectral wavelengths. Three specific spectral wavelengths (490 nm, 550 nm and 610 nm) were chosen for illustrative purposes to highlight key differences between the tested methods (see Fig. 4.6).

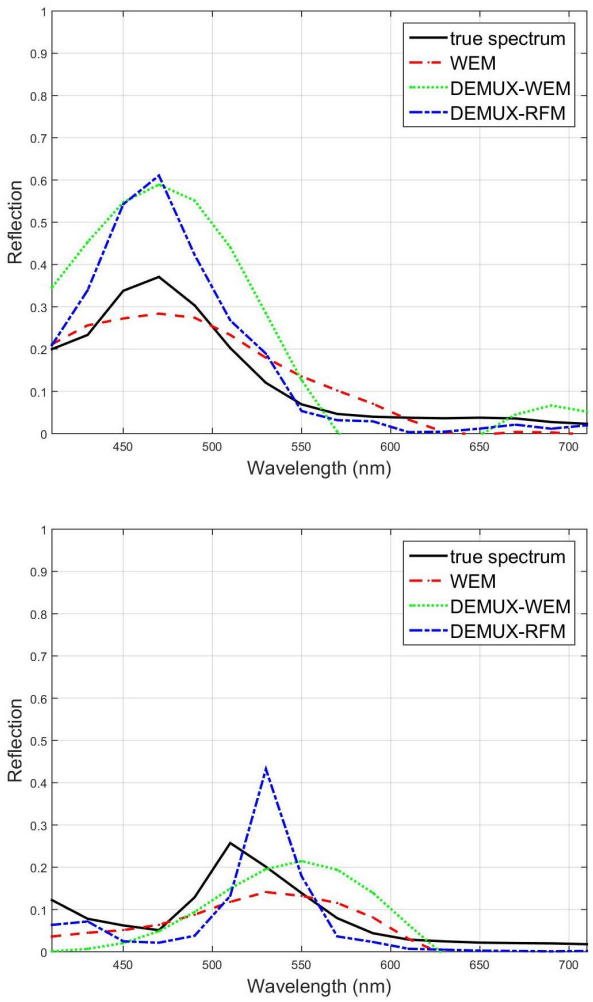

Figure 4.4: Two of the five true reflectance spectra ('blue' and 'green') from the test icon (see Fig. 4.3), along with the corresponding predicted spectra obtained from a state-of-the-art Wiener Estimation Method (WEM), the proposed Wiener-based demultiplexer (DEMUX-WEM) and the random forest-based demultiplexer (DEMUX-RFM). Top: The 'blue' true spectrum and the predicted spectra produced using the inverse methods have similarly shaped spectral curves. Bottom: the predicted spectra from DEMUX-RFM is closest to the true 'green' spectrum.

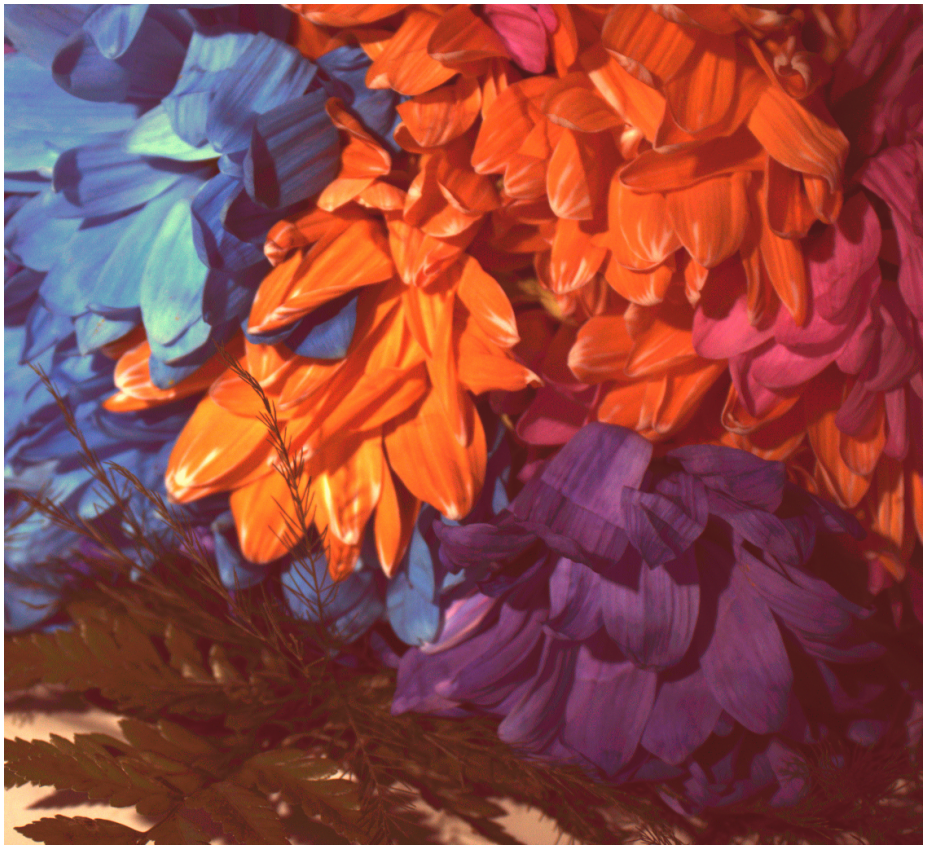

Figure 4.5: Sensor measurements of a scene consisting of flowers of different colors using real spectrally-characterized Canon T3i sensor with a Bayer pattern CFA used in the second set of experiments.

4.4.2 Results

The predicted spectral images at three different spectral wavelengths (490 nm, 550 nm and 610 nm) were obtained using the WEM, DEMUX-WEM, and DEMUX-RFM methods for a scene consisting of flowers with different colors as shown in Fig. 4.6. A number of interesting observations can be made from the predicted spectral images. It can be observed that Flower A can be seen to have noticeably higher intensities at 490 nm for the DEMUX-WEM and DEMUX-RFM methods, particularly with higher intensity contrast between Flower A and the other flowers, when compared to the WEM method. Since Flower A is a blue flower it has a significantly higher reflectance at 490 nm compared to the other flowers. This illustrates the efficacy of the proposed DEMUX-WEM and

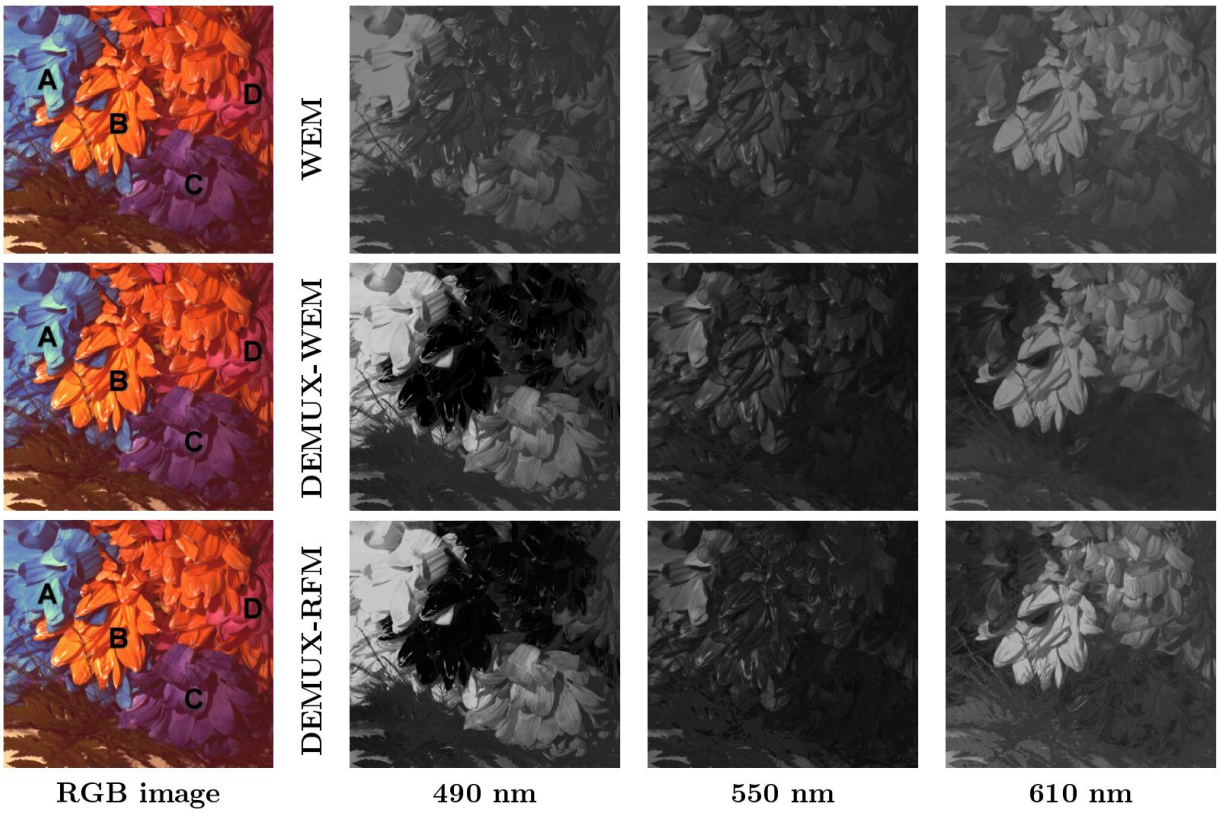

Figure 4.6: Predicted reflectance spectra images at three specific spectral wavelengths (490 nm, 550 nm and 610 nm) for the scene of flowers with different colors used in the second set of experiments. The three specific wavelengths are chosen for illustrative purposes to highlight key differences between the tested methods.

DEMUX-RFM methods in this case.

It can also be observed that Flower B has a very low intensity at 490 nm for the DEMUX-WEM and DEMUX-RFM methods, while the WEM method shows noticeably higher relative intensity at 490 nm in comparison. Given that Flower B is an orange flower and has very low reflectance at 490 nm, the predicted reflectance spectra produced by the DEMUX-WEM and DEMUX-RFM methods more accurately represent the scene compared to the WEM method. Furthermore, it is interesting that there is noticeably higher contrast between Flower B and Flower D at both 490 nm and 610 nm with the proposed DEMUX-WEM and DEMUX-RFM methods compared to the WEM method. In particular, Flower B and Flower D are visually inseparable from the spectral image

produced using WEM at 610 nm. In addition, Flower B is orange and exhibits higher reflectance than Flower D at 610 nm, since 610 nm corresponds to the orange portion of the visible band. These improved reflectance spectra predictions illustrate the efficacy of the proposed DEMUX-WEM and DEMUX-RFM methods.

It can be further observed that Flower B has a noticeably higher intensity at 610 nm for the DEMUX-RFM method when compared to both DEMUX-WEM and WEM, with noticeably greater contrast between Flower B and other flowers at 610 nm when compared to DEMUX-WEM and WEM. Given that Flower B is an orange flower and exhibits higher reflectance at 610 nm (orange color in the visible spectrum), the superior performance of the proposed DEMUX-RFM method is demonstrated compared to the other methods.

Finally, Flower C has noticeably higher intensity at 610 nm for DEMUX-RFM compared to DEMUX-WEM, and noticeably lower intensity at 550 nm for DEMUX-RFM compared to WEM. Given that Flower C is a purple flower and is characterized by high reflectance at 490 nm, very low reflectance at 550 nm, and mild reflectance at 610 nm, the results of DEMUX-RFM are more representative of the reflectance spectra of Flower C compared to DEMUX-WEM and WEM.

4.5 Discussion

The three different methods (WEM, DEMUX-WEM, and DEMUX-RFM) were evaluated using three different tests to determine the relative performance of each inverse process. These tests were run to determine both the quantitative and qualitative performance of each method.

Comprehensive quantitative performance assessment within a controlled simulation environment as well as with real-world measurements of a test icon demonstrate the efficacy of the proposed framework. The experimental results demonstrate that such an approach can be used to enable simultaneous multispectral imaging using conventional image sensors with standard CFAs. The numerical demultiplexing method works in scenarios when the reflectance spectra of the samples being imaged are typical and constrained in both diversity and anomalous peculiarities, which is true for a wide range of specific applications.

The noticeable PSNR gains achieved while using the proposed framework may stem from the fact that a comprehensive spectral characterization of the detector was introduced to obtain an accurate computational forward model, which was then used to build a numerical demultiplexer. This differs from the previously proposed Wiener estimation method which aims to learn a parametric statistical model that maps sensor measurements

to input light spectra directly using spectral characterization information. By first building a more accurate computational forward model, which is based on the spectral characterization of the image sensor, a more accurate numerical demultiplexer can be constructed. This numerical demultiplexer can in turn predict a greater variety of reflectance spectra in a more reliable manner. This factor is reinforced by the first experimental results, where both of the proposed numerical demultiplexers (DEMUX-WEM and DEMUX-RFM) performed noticeably better than the Wiener estimation method (WEM) when tasked to predict a wide variety of reflectance spectra.

A key factor to the noticeable PSNR gains achieved using the proposed method (DEMUX-RFM) when compared to the alternate proposed method (DEMUX-WEM) may stem from the fact that a non-linear random forest model was used to construct the numerical demultiplexer. This non-linear inverse model is less prone to overfitting and more flexible than the parametric statistical model used in Wiener-based methods. This allows for a more robust and generalized demultiplexer that performs well for predicting a greater diversity of reflectance spectra and is less sensitive to illumination variations. This factor is reinforced by the experimental results from both sets of experiments, which showed that the proposed random forest-based numerical demultiplexer (DEMUX-RFM) performs noticeably better than the proposed Wiener-based numerical demultiplexer (DEMUX-WEM).

As we have demonstrated in this study, demultiplexing of RGB color sensor measurements into higher spectral signals is possible via a numerical demultiplexing. This simultaneous multispectral imaging method has strong implications for many applications where low-cost, low-complexity, and portable simultaneous multispectral imaging systems are highly desired. Two of these applications include photoplethysmogrpahic imaging and multispectral microscopy, which will be discussed in the next two chapters.

Chapter 5

Application: Photoplethysmographic Imaging

Having constructed the numerical spectral demultiplexer (NSD) we now use it for photoplethysmographic imaging (PPGI), which is a non-invasive method to detect a cardiovascular pulse wave travelling through the body [37]. By inferring narrow-band spectral information from acquired broadband RGB measurements we are able to estimate heart rate via the computation of motion-compensated skin erythema fluctuation analysis. We then compare the NSD erythema fluctuation analysis (NSDEFA) against the baseline method of erythema fluctuation analysis (EFA) and show that the NSDEFA performs better than the EFA.

5.1 Introduction

The advent of consumer digital cameras has led the way to digitizing information in the form of photographs or videos which adhere to the human vision model of the red-blue-green (RGB) color information. Recently, these digital cameras have been used for photoplethysmographic imaging (PPGI). One method to find a PPG signal is to extract the RGB frames by selecting a single color channel, which is often green or red. [38, 39, 40]. Other studies have used optical components to control the spectral input. For example, narrow bandpass filters were used on separate cameras for concurrent spectral processing [41]. Other studies have proposed a transformation of RGB to a more representative color space. Independent component analysis was proposed with the assumption that one of the

independent components represented the intensity fluctuations due to blood pulsing [42]. A log-ratio formulation based on a Beer-Lambert law derivation in RGB was proposed to approximate the blood pulse waveform [43].

Some studies have explored more fine-grained spectral analysis than the traditional RGB decomposition. A five-band spectral grid filter was proposed to replace the standard Bayer filter [44]. The best combination was cyan, green, and orange responses, which varied from the traditional RGB selection process. However, there has been little research done to decompose the image into fine-grained spectral components using software.

In this work we propose a novel numerical spectral demultiplexing (NSD) method to infer narrow-band spectral information from acquired broadband RGB measurements in order to estimate heart rate via the computation of motion-compensated skin erythema fluctuation analysis. This new method, NSD erythema fluctuation analysis (NSDEFA), will be compared to the baseline method of erythema fluctuation analysis (EFA) [45].

5.2 Methodology

As seen in Figure 5.1, the methodology consists of three main steps which are: 1) extract the RGB signal from the video (Section 5.2.1), 2) demultiplex the RGB values into narrow-band spectral signals (Section 5.2.2), and 3) use the demultiplexed signals to calculate the erythema fluctuation (Section 5.2.3).

5.2.1 Signal Extraction from Video

To acquire signals which are robust to temporal noise and natural human motion, a single point, $\underline{x}$, is selected and tracked throughout the video sequence, as seen in Figure 5.2. The point tracking is formulated as

$$\underline{x}_t = f(\underline{x}_{t-1}) \tag{5.1}$$

where $f(\underline{x}_{t-1})$ is the point tracking function (i.e., Kanade-Lucas-Tomasi algorithm [46]). To mitigate the effects of point noise and tracking error, an $n \times n$ pixel window centred at $\underline{x}$ is sampled at a given time, t:

$$r(t) = E(r|\Omega(\underline{x}_t)) \qquad g(t) = E(g|\Omega(\underline{x}_t)) \qquad b(t) = E(b|\Omega(\underline{x}_t)) \tag{5.2}$$

subject to

$$r(t_0) = E(r|\Omega(\underline{x}_{t_0})) \qquad g(t_0) = E(g|\Omega(\underline{x}_{t_0})) \qquad b(t_0) = E(b|\Omega(\underline{x}_{t_0})) \tag{5.3}$$

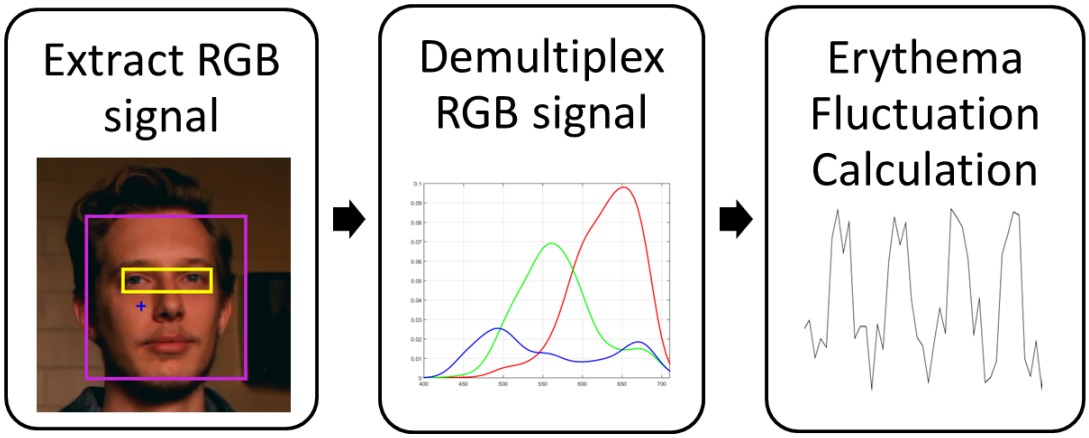

Figure 5.1: The numerical spectral demultiplexing erythema fluctuation analysis (NSDEFA) method is broken down into three stages. First, the RGB signal is extracted from a video and then demultiplexed into narrow-band signals. Using this new signal the erythema fluctuation calculation is done.

where $\underline{x}_{t_0}$ is the location of the initial sample point, $\Omega(\underline{x})$ is the set of pixels within the $n \times n$ sample region surrounding $\underline{x}$, and $r(t)$, $g(t)$ and $b(t)$ are the expectation (denoted here as $E(.)$) of the red, green and blue channel values, respectively, given $\Omega(\underline{x}_t)$.

To ensure the sample point provides relevant heart rate signals, the subject's face, eyes, are first registered via the Viola-Jones face detection algorithm [47]. The initial sample location, $\underline{x}_{t_0}$, is determined with respect to these sub-features, as seen in Figure 5.2, and is selected to be on the subject's cheek region due to low facial skin thickness [48], lack of occluding features (i.e., facial hair and hats), and relative flatness of the area. Similar to Chung *et al.* [45], this point sampling and tracking is repeated at 10 different locations to mitigate the effects of noise and subject motion.

5.2.2 Numerical Spectral Demultiplexing

The numerical demultiplexing system (NDS) that was described in Chapter 3 was used to create the NSD erythema fluctuation analysis (NSDEFA) method. This method was trained using the 10,000 spectra to RGB mappings created by the forward model as described in Section 3.2. A Canon T3i APS-C CMOS image sensor was used to capture the videos in order to demultiplex the colour image sensor measurements into higher spectral signals.

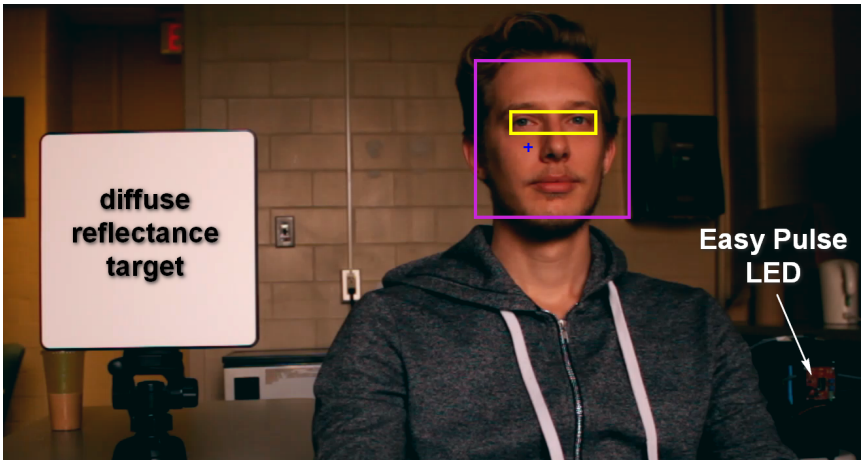

Figure 5.2: For a given video, the participant wore an Easy Pulse sensor on their finger which sent the heart rate signal to the Easy Pulse LED. The RGB signal (blue +) was extracted from the relative position of the subject's face (magenta box) and eyes (yellow box), and then demultiplexed into narrow-band signals at 545 nm for green and 640 nm for red. These narrow-band green and red signals were then used to find a more accurate erythema fluctuation value. A diffuse reflectance target was included in the scene for white balance correction.

5.2.3 Erythema Fluctuation Calculation

The subject's heart rate is extracted via skin erythema fluctuation analysis in the same manner as the baseline EFA method from Chung *et al.* [45]. Skin erythema has excellent linearity with hemoglobin concentration, and Gong *et al.* [49] proposed the following equation for the quantification of hemoglobin and melanin via skin erythema values:

$$e(t) = \log_{10} \frac{1}{g(t)} - \log_{10} \frac{1}{r(t)} \tag{5.4}$$

where $r(t)$ and $g(t)$ are the spectrally demultiplexed red and green narrow-band signals, respectively. Given the time series of skin erythema $e(t)$, the frequency representation of the erythema signal $\Phi(u) = \mathcal{F}\{e(t)\}$ can be analysed to determine an estimation of the subject's heart rate:

$$u_{\text{HR}} = \arg\max_{u} \ |\Phi(u)| \qquad \text{subject to} \qquad \alpha \leq H(u) \leq \beta \tag{5.5}$$

where $H(u) = 60u$ is a function for converting frequency (Hz) to heart rate (bpm).

Table 5.1: The relative errors of the baseline EFA method [45] and the proposed NSDEFA method were calculated for 26 different videos. The NSDEFA has a lower average relative error compared to the baseline EFA method.

Video Number	**Ground Truth (bpm)**	**EFA [45] (bpm)**	**NSDEFA (bpm)**	**EFA error**	**NSDEFA error**
1	60.4	59.9	56.4	**0.008**	0.067
2	62.4	62.8	57.6	**0.005**	0.078
3	59.2	61.6	58.5	0.041	**0.011**
4	64.1	60.2	66.7	0.062	**0.041**
5	68.9	48.7	63.6	0.292	**0.076**
6	65.9	62.0	62.9	0.060	**0.047**
7	81.1	76.0	81.2	0.063	**0.001**
8	84.1	76.4	73.9	**0.092**	0.121
9	80.0	57.3	58.6	0.284	**0.267**
10	62.0	65.8	60.1	0.061	**0.030**
11	57.6	57.5	60.8	**0.001**	0.056
12	59.1	52.0	59.5	0.121	**0.006**
13	56.9	54.7	58.4	0.039	**0.026**
14	57.5	54.8	57.8	0.048	**0.006**
15	88.5	62.8	67.4	0.291	**0.238**
16	86.4	72.2	67.1	**0.165**	0.224
17	95.8	65.1	75.1	0.321	**0.216**
18	94.6	72.3	72.5	0.236	**0.233**
19	93.0	56.7	59.2	0.391	**0.364**
20	94.6	86.6	54.5	**0.085**	0.425
21	61.3	75.4	67.8	0.230	**0.105**
22	68.6	74.8	71.3	0.091	**0.039**
23	79.3	80.0	70.5	**0.010**	0.111
24	81.5	68.8	67.4	**0.156**	0.172
25	90.1	64.5	72.1	0.284	**0.199**
26	66.2	78.3	67.4	0.183	**0.018**
			AVERAGE	0.137	**0.126**

The average resting heart rate is between 60 bpm and 100 bpm [50], with well-trained athletes having an average resting heart rate as low as 40 bpm. As in the original EFA

method [45], the lower limit α is set to 40 bpm and the upper limit β is set to 100 bpm. The bpm corresponding to the highest amplitude within the range of plausible heart rates in the frequency domain is selected as the subject's estimated heart rate HR, i.e., $\text{HR} = H(u_{\text{HR}})$.

5.3 Results

In order to evaluate the efficacy of the proposed method for improving the prediction of heart rate estimation, we ran a set of experiments where we captured 26 videos of five different participants (authors JD, AC, BC, RA, and AW), each 30 seconds long, using the setup shown in Figure 5.2. Each participant wore an Easy Pulse sensor on their finger that was connected to a red LED which flashed in time with the participants heart rate. This LED was included in the field of view of each video in order to extract ground truth heart rate measurements. A diffuse reflectance surface was also included in the field of view of each video for white balance correction. All scenes where illuminated by ambient daylight.

To compare the predicted heart rate against the ground truth heart rate we calculated the relative error for both the original EFA method [45] that uses the green and red pixel values, as well for the proposed method NSDEFA, which uses the inferred narrow-band signals at 545 nm for green and 640 nm for red. As seen in Table 5.1, the average relative error for the EFA method was 0.137 while the average relative error for the NSDEFA method was lower at a value of 0.126. Out of 26 videos the NSDEFA had a lower relative error 18 times compared to the the EFA method.

5.4 Conclusion

In this chapter, we show that we can predict heart rate estimation using a numerical spectral demultiplexing (NSD) method to infer narrow-band spectral information from acquired broadband RGB measurements. The motion-compensated RGB signal were spectrally demultiplexed using a non-linear inverse model based on the spectral sensitivity of the camera's sensor. These demultiplexed signals were then used to find a more accurate heart rate estimation via narrow-band erythema fluctuation analysis compared to using just the green and red broadband measurements. The average relative error for the proposed NSDEFA method (0.126) is lower than the baseline EFA method (0.137). Therefore, decomposing the RGB camera measurements into narrow-band spectral information can improve the prediction of heart rate estimation. Finally, since generalized spectra were used to train the NSD system, additional priors of the spectra of human skin could be used in the future to further improve the accuracy of the erythema fluctuation when using the numerical demultiplexing system.

Chapter 6

Application: Multispectral Microscopy

The numerical spectral demultiplexer (NSD) that was used for photoplethysmographic imaging (PPGI) can also be used for multispectral microscopy. We use a numerical spectral demulitplexing microscopy (NSDM) system to predict narrow-band spectra from RGB broadband measurements and use this method for dark-field and bright-field microscopy.

6.1 Introduction

Microscopes are optical instruments which allow scientists to study and observe objects on the micron and nano scale. Biologists, chemists, and other scientific disciplines greatly benefit from microscope systems since they magnify objects which are invisible to our human eyes. A wide range of microscopy techniques exists and include light-field and dark-field microscopy, fluorescence microscopy, confocal microscopy, and even lensless microscopy. Each of these different techniques uses different light sources, such as lasers or light emitting diodes (LEDs), as well different lensing configurations, and therefore each has its own advantages and disadvantages.

Often times a digital imaging system will be mounted to a microscope to gather observations and measurements of a variety of specimens. However, most digital microscopy systems captures spectral data in a limited number of wavelength bands which results in limited spectral information about the specimen. Moreover, when a multispectral microscope captures multiple spectral bands using a variety of light sources or optical filters,

it is usually done in a sequential manner, which prevents capturing transient phenomena when imaging in vivo samples. These systems quickly become very large and expensive which limits their mobility and accessibility.

To combat the issues that arise when sequentially capturing multispectral data, one approach is to capture broadband signals simultaneously using a consumer three-band red, green, and blue (RGB) camera, and then infer additional spectral information during the post-processing of the imaging data. At present only one method exists that infers spectral information from RGB broadband measurements based on the spectral sensitivity of the camera sensor, known as Wiener estimation. This method shows significant promise, however, it comes with its own limitations. We propose to use a new method to predict narrow-band spectra from RGB broadband measurements and use this method for microscopy applications. We call this method Numerical Spectral Demulitplexing Microscopy (NSDM). It allows for a low-cost, portable multispectral microscope, which can be used for point of care application.

In Section 6.2 we discuss the state of the art work in multispectral microscopy and in Section 6.3 we go into detail about our NSDM proposed system. In Section 6.4 we show our results by imaging two botanical specimens using a bright-field microscope as well as two anatomical specimens using both a bright-field microscope and a dark-field fluorescence microscope. Finally, in Section 6.5, we discuss our conclusions.

6.2 Related Work

Most multispectral microscopy systems have sequential image capture for each spectral image and require complicated equipment and therefore are usually large and expensive. Dickinson et al. [51] accomplish multispectral laser scanning fluorescence microscopy by capturing a spectral images sequentially in time, and then use linear unmixing to create multi-fluorescence images with clear separated image channels representing one fluorochrome each. The linear unmixing is accomplished based on the a priori knowledge of the expected spectral signatures of each individual fluorochrome.

Levenson et al. [52] discuss methods of multispectral microscopy which include attachments for a standard C-mount equipped microscope. Using this multispectral imaging system also requires taking a series of images for different wavelengths to build up the lambda stack.

Finally, Adams et al. [53] use lasers for a high-speed multispectral spinning-disk confocal microscope system for fluorescent speckle microscopy of living cells. Once again, the dual-

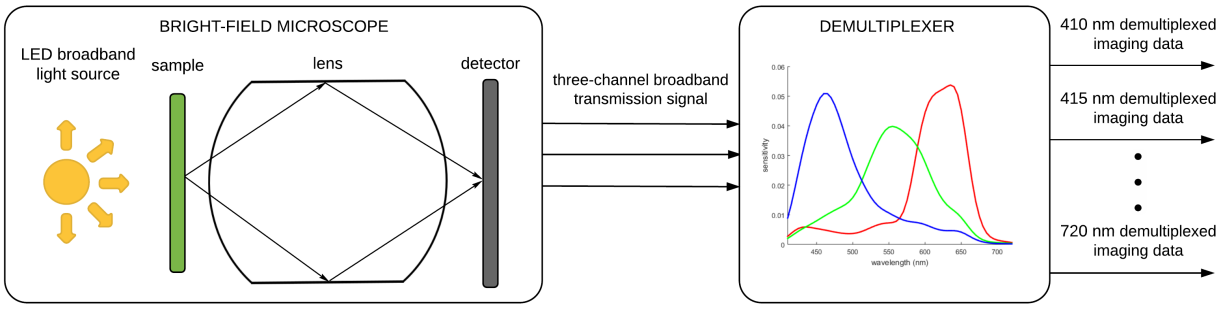

(a) Bright-field Numerical Spectral Demulitplexing Microscope (NSDM)

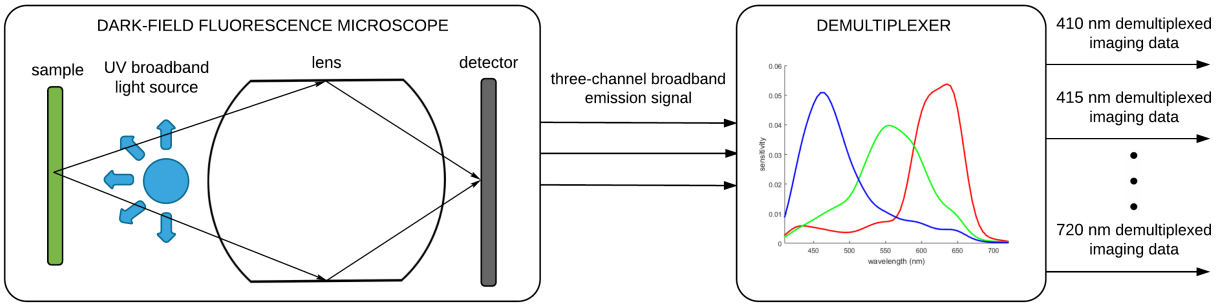

(b) Dark-field Fluorescence Numerical Spectral Demulitplexing Microscope (NSDM)

Figure 6.1: A digital microscope was built using the Raspberry Pi camera and a simple lens. This microscope can operate as (a) a bright-field microscope as well as (b) a dark-field fluorescence microscope, depending on the location and type of light source. In the case of (a) the broadband signal is the transmission of visible light through the sample and in (b) it is the emission of visible light from the sample. The three channel broadband measurements of the bright-field or dark-field fluorescence microscope system are fed into the demultiplexer which takes the RGB measurements and predicts narrow-band spectral signals from 410 nm - 720 nm, with a resolution of 5 nm. This numerical demulitplexer is trained based on the a priori knowledge of the camera spectral sensitivity of the RGB channels.

spinning-disk requires the specimens to be imaged sequentially for each unique excitation wavelength.

A more recent development in low-cost multispectral microscopy is employing an array of LEDs for imaging broad-band transmission spectroscopy, as proposed by Brydegaard et al. [15]. Brydegaard et al. use a modified commercial bright-field microscope equipped with a CMOS sensor and combined it with an array of LEDs with emission from the UV to

the NIR. Using this system they captured 13 quasi-monochromatic wavelength images and were able to validate their system by imaging different types of vegetation. At a later date Brydegaard et al. [54] extended their work to include a reflection multispectral microscope. Other research by Everdell et al. [55] also uses LED illumination for obtaining sequential multispectral optical images of the human ocular fundus.

All these methods require sequential image capture for each illuminated wavelength band, and cannot capture transient phenomena, which is a major system limitation. Therefore a simultaneous multispectral imaging technique is highly desirable. One technique that shows promise is the Wiener estimation method which infers spectral information from a consumer RGB camera based on the spectral sensitivity of the sensor, as proposed by Stigell et el. [24]. Chen et al. [26] use a modified Wiener approach to predict the diffuse reflection of tissue measurements while Orava et al. [56] use the Wiener method to predict the spectral reflection of minced meat in order to determine its quality during storage. More recently Nishidate et al. use this method to estimate the melanin and hemoglobin from human skin measurements [25] as well as to determine in vivo scattering and absorption of exposed rat brain tissue [57].

Taking this into consideration we propose a new method to infer multispectral data from a RGB camera and use it to create a multispectral microscope and all this system numerical spectral demultiplexing microscopy (NSDM) which does not make any underlying assumptions about the data. NSDM uses a non-linear inverse model to predict the spectra given the RGB measurements of the camera, which allows for a low-cost, simultaneous multispectral microscopy system. Furthermore, we show that this system can be used for bright-field multispectral microscopy as well as dark-field multispectral fluorescence microscopy.

6.3 Methodology

The proposed numerical spectral demultiplexing microscopy (NSDM) system consists of two main components, as shown in Figure 6.1. The first component is the microscopy instrument which is used to obtain a three-channel broadband light measurement using a Raspberry Pi camera and a simple lens (Section 6.3.1). The second component is the numerical spectral demultiplexer, which is used to demultiplex the RGB multiplexed broadband imaging signals into a series of demultiplexed narrowband imaging data at different wavelengths using an inverse regression model created from the spectral characterization of the detector (Section 6.3.2).

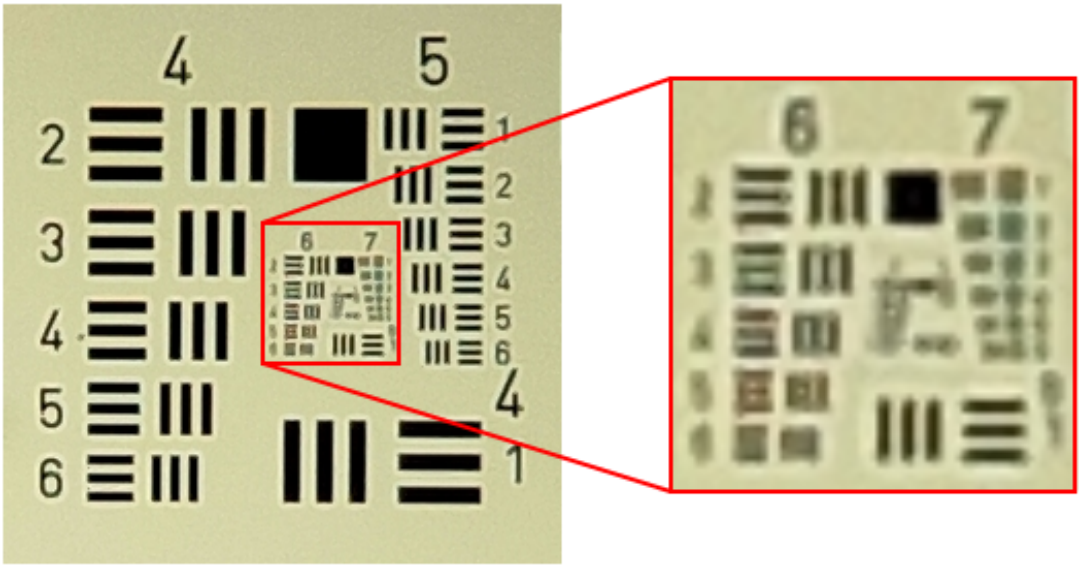

Figure 6.2: By using the 1951 U.S. Air Force (USAF) target, the spatial resolution of the numerical spectral demulitplexing microscope (NSDM) was determined to be 2.76 μm.

6.3.1 Microscopy instrument

As the first component of the NSDM system, we built a microscopy instrument using the Raspberry camera system due to its portability and low cost. To turn this camera into a digital microscope a cemented achromatic doublet lens with a focal length of 10 mm and a diameter of 8 mm was placed in the optical path of the Raspberry Pi camera.

As seen in Figure 6.1, this microscope system can act as a bright-field microscope (Figure 6.1a), or as a dark-field fluorescence microscope (Figure 6.1b). For the bright-field microscope a broadband LED light source was placed behind the specimen and the transmission of light through the specimen was measured by the sensor. On the other hand, a broadband UV light source was placed between the sample and the lens to create a dark-field fluorescence microscope. The sample absorbs the UV light and emits light in the visible range (420 nm - 720 nm), which is measured by the Raspberry Pi camera.

The spatial resolution of the constructed microscopy instrument was measured by imaging a 1951 U.S. Air Force (USAF) resolution test chart, as seen in Figure 6.2. Both the horizontal and vertical lines were distinguishable in group 6 element 4, with a line width of four pixels. Therefore each pixel is 1.38 μm across and the imaging resolution is 2.76 μm.

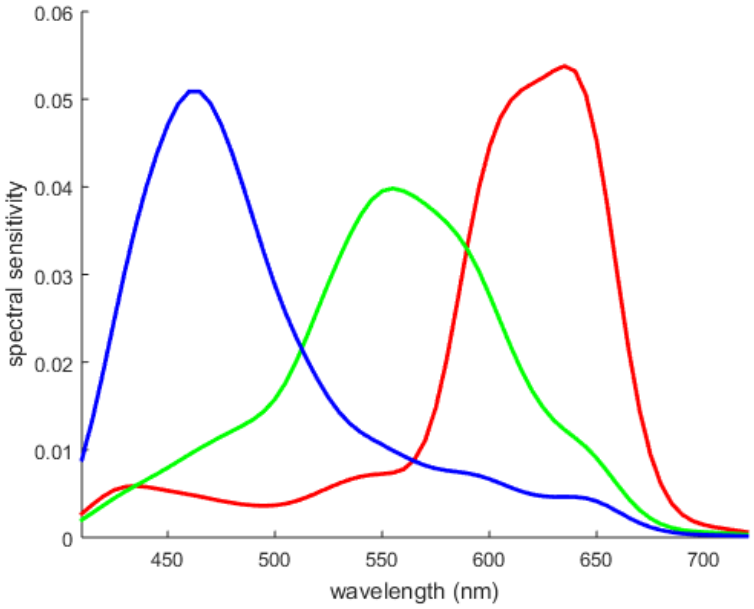

Figure 6.3: The spectral sensitivity of the Raspberry Pi camera was measured from 410 nm - 720 nm with 5 nm resolution using a monochrometer. These spectral sensitivity curves were used to build a forward model which mapped generated spectra to RGB values. This forward model was then used to train an inverse non-linear random forest model allowing us to create a spectral demultiplexing system which predicts narrow-band spectra signals based on the RGB pixel values of a microscope image.

6.3.2 Numerical Spectral Demultiplexer

The second component is the numerical spectral demultiplexer, which is used to demultiplex the multiplexed broadband RGB signals into a series of demultiplexed narrow-band imaging signals at different wavelengths using an inverse regression model created from the prior knowledge of the spectral characterization of the detector.

The Numerical Demultiplexing System (NDS) that was described in Chapter 3 was used to to create the multispectral microscope with the expection that a Raspberry Pi camera was used instead of the Canon Rebel T3i camera. The spectral sensitivity of the Raspberry Pi camera was measured using a monochrometer from 420 nm - 720 nm at a resolution of 5 nm, resulting in 63 measurements. The raw spectral sensitivity data was smoothed to remove any noise in order to find the RGB channels of the Raspberry Pi camera, as seen in Figure 6.3.

To create a training set, 15000 different Λ vectors were generated using a mixed Gaussian model. For each of the 15000 Λ vectors, a range of one to five Gaussian curves with randomly chosen variance and mean were added together. These 15000 different Λ vectors were then mapped to 15000 RGB values using the forward model of the Raspberry Pi camera. Since we are training with generalized spectra, and not with unique spectra determined from the microscope specimens, we hope to achieve representative spectra without additional prior information.

6.4 Results

We can now use the trained inverse model, as fully described in Chapter 3, to generate 63 narrow-band wavelength measurements from the RGB broadband measurements which will result in a unique spectra at each pixel for a microscope image. This will be done for bright-field microscopy images of botanical specimens (Section 6.4.1) as well as bright-field and dark-field fluorescence images of anatomical specimens (Section 6.4.2).

6.4.1 Bright-field Multispectral Microscopy for Botanical Specimens

The transmission spectra at each pixel was predicted for two botanical specimens by imaging the specimens using the bright-field NSDM system (Figure 6.1a). The first specimen was a corn seed with endosperm (Figure 6.4a) and the second specimen was a pinus male strobilus, or a male pine cone (Figure 6.4b).

From Figure 6.4 we show that a multispectral bright-field microscopy with instantaneous capture is possible using a low-cost consumer camera. This allows inspection of the spectral makeup of different parts of these botanical specimens, which can provide insight to the structure and functionality of these specimens.

6.4.2 Bright-field Multispectral Microscopy and Dark-field Fluorescence Multispectral Microscopy for Anatomical Specimens

Using both the bright-field NSDM system (Figure 6.1a) and the dark-field fluorescence NSDM (Figure 6.1b) images were taken of different anatomical specimens. The first images

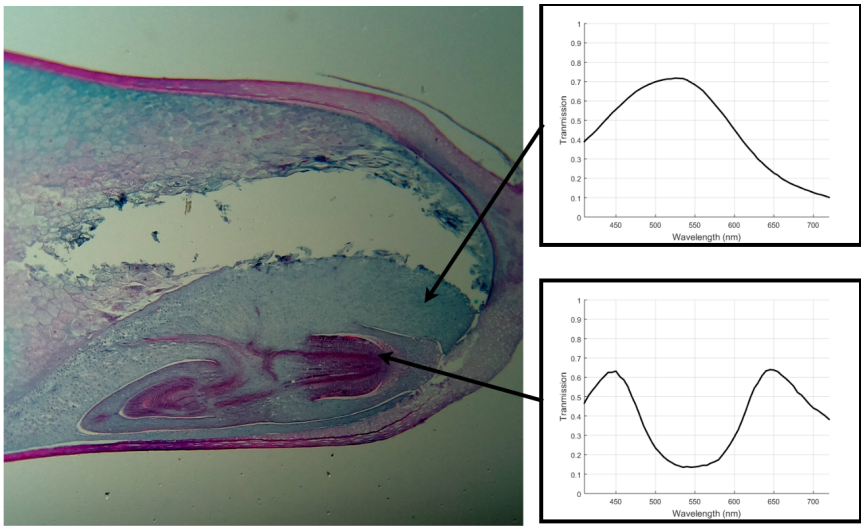

(a) Corn Seed Bright-field Microscope Image

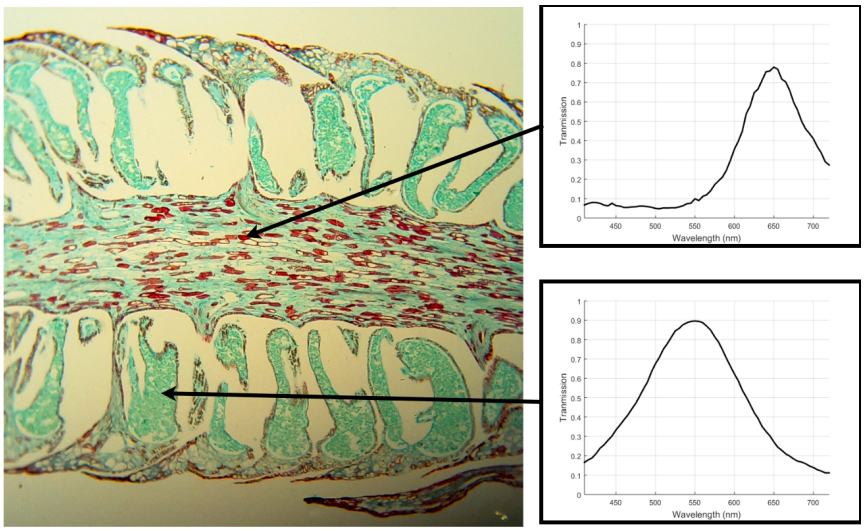

(b) Pinus Male Strobilus Bright-field Microscope Image

Figure 6.4: The Numerical Spectral Demultiplexing Microscope (NSDM) was used to take bright-field microscopy images of botanical specimens which include (a) a corn seed, and (b) a pinus male strobilus (male pinecone). In both of these images the predicted transmission spectra at different pixel locations can be seen on the right. By inferring the transmission spectra of the entire RGB image, we are able to build a multispectral microscopy system.

are of a ureter specimen (Figure 6.5) and the second images are of a islet of Langerhans region of the pancreas (Figure 6.6).

The transmission spectra at two different pixels of the ureter can be seen in Figure 6.5a. By comparing these two spectra it is observed that they are very similar in nature, and are therefore not separable. However, if we inspect the same pixels in the reflection spectra of the dark-field fluorescence image (Figure 6.5b), we can see that the pixels become more separable.

Similarly, as seen in Figure 6.6a, the predicted transmission spectra at two different pixels of the islet of Langerhans region bright-field image are very similar and therefore no new information can be gained. Once again, as seen in Figure 6.6b, the predicted reflection spectra at these same two pixels are much different in the dark-field fluorescence image. This illustrates that additional information can be gathered by combining a bright-field NSDM system with a dark-field fluorescence NSDM system.

6.5 Conclusions

In this chapter we introduced the numerical spectral demultiplexing microscopy (NSDM) system which took a normal digital microscope and transformed it into a multispectral microscope by demultiplexing the broadband RGB signals into narrow-band spectra. This demultiplexing was accomplished by training a non-linear random forest regression model based on the spectral sensitivity of the Raspberry Pi camera. The NSDM system was used as both a bright-field multispectral microscope as well as a dark-field fluorescence multispectral microscope, which illustrates its potential as a low-cost, portable, point of care system.

Furthermore, the fact that we trained the inverse model using a generalized spectra, which based on a mixed Gaussian model, illustrates the strength in the numerical demultiplexer since it can create realistic spectra without adding new priors about the spectra of the microscope specimens. However, if such priors where added, one would anticipate more representative spectra of the specimens. Finally, initial results from the NSDM system shows promise that converting the RGB measurements into a 63 dimensional spectra space allows for more separability of classes. A further pattern recognition study would yield beneficial to determine how separable different classes would be in the higher-dimensional spectral space.

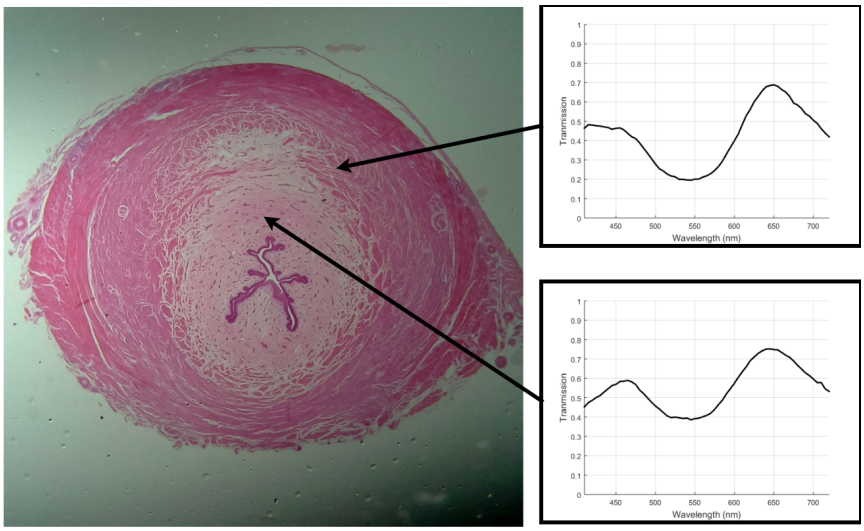

(a) Ureter Bright-field Microscope Image

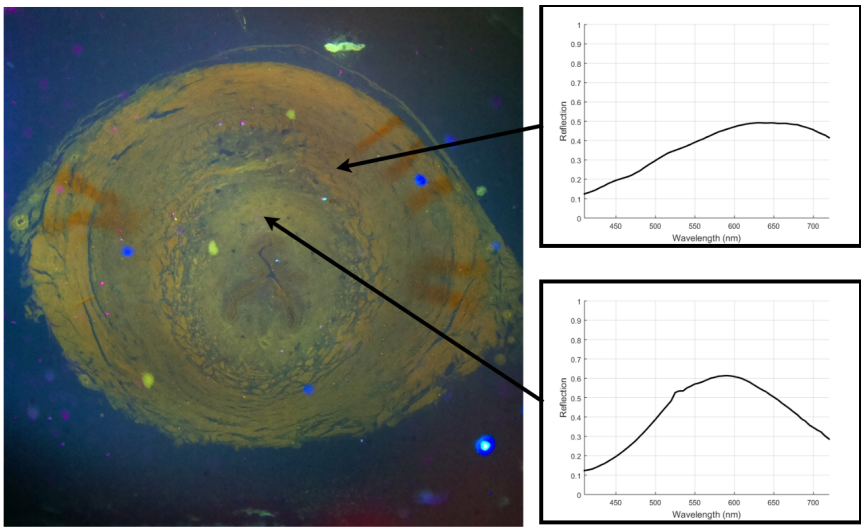

(b) Ureter Dark-field Fluorescence Microscope Image

Figure 6.5: The numerical spectral demulitplexing microscope (NSDM) was used to capture images of a ureter using (a) a bright-field microscope and (b) a dark-field fluorescence microscope. From inspecting (a) we observe that different parts of the anatomical specimen have very similar predicted spectra. However, when observing (b) the same pixel locations have much different predicted spectra. Therefore, by using dark-field fluorescence microscopy we gain valuable information about the specimen.

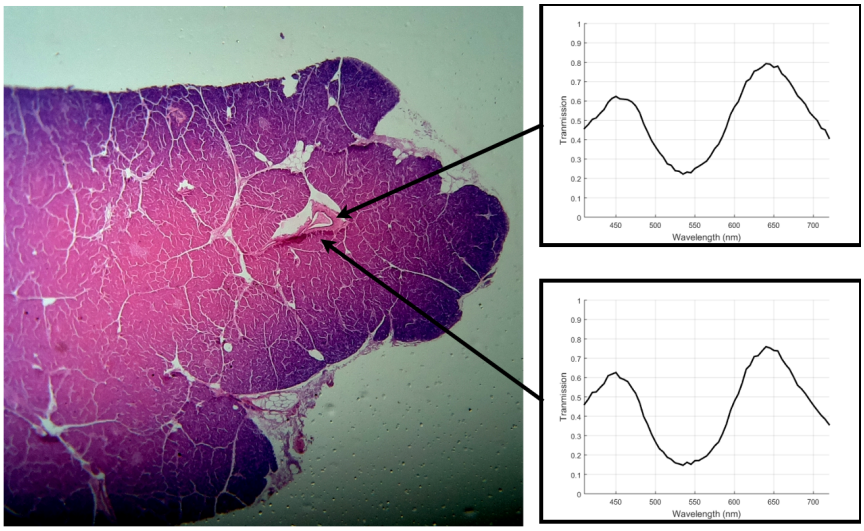

(a) Islet of Langerhans Region of the Pancreas Bright-field Microscope Image

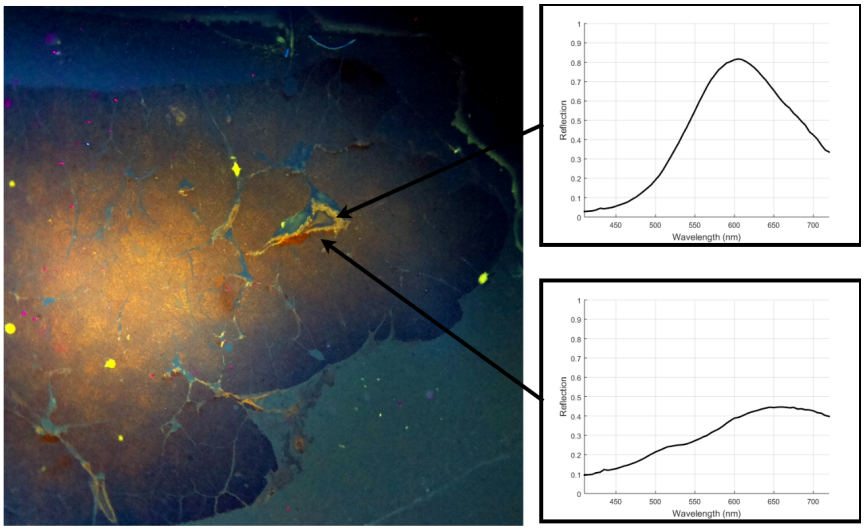

(b) Islet of Langerhans Region of the Pancreas Dark-field Fluorescence Microscope Image

Figure 6.6: The numerical spectral demulitplexing microscope (NSDM) was used to capture images of the islet of Langerhans region of the pancreas using (a) a bright-field microscope and (b) a dark-field fluorescence microscope. In (a) we observe that different parts of the anatomical specimen have very similar predicted spectra. However, when observing (b) the same pixel locations have much different predicted spectra. This illustrates that additional information can be gathered by combining a bright-field NSDM system with a dark-field fluorescence NSDM system.

Chapter 7

Conclusions

Consumer digital cameras with a Bayer filter are becoming more common place due to decreases in manufacturing costs and increases in accessibility. Traditional multispectral imaging devices that use filter wheels and tunable filters are able to capture higher spectral content than a standard consumer digital camera. However, they are considerable more expensive and require sequential capture for the different wavelength bands. This reduction in temporal resolution makes imaging dynamic or transient phenomena much more challenging. Therefore there is a need for a simultaneous multispectral imaging system which would facilitate the capture of dynamic or transient phenomena at multiple wavelengths. An effective method to accomplish this is to use a Bayer CFA and infer higher spectral content. While this approach is not as flexible and reliable as pure spectroscopy, it has been effectively used in a wide range of applications such as artwork assessment [23, 28], clinical skin imaging [25], vein visualization [30], hemodynamic visualization [31], and microscopy [16]. Currently the main method to predict higher spectral from a Bayer CFA is known as Wiener estimation. This method uses auto-correlation and cross-correlation are used to statistically model the relationship between the incoming light spectra and the image sensor measurements [23, 24, 25, 26, 27, 28]. However, these inherent statistical assumptions limit the ability to predict the incoming spectra.

This thesis has shown a more reliable method of inferring the incoming spectra using a conventional RGB Bayer CFA. This is accomplished by first characterizing the spectral sensitivity of the Bayer CFA and using this as a forward model to generate 10,000 spectra to RGB pairs. This set of data are then used to train a non-linear random forest inverse model. When comparing the proposed DEMUX-RFM against the state of the art Wiener Estimation (WEM), it was shown that the DEMUX-RFM outperforms the WEM in both simulated and real-world test. Therefore the DEMUX-RFM allows for a more robust and

generalized demultiplexer that is able to predict a greater diversity of reflectance spectra and is less sensitive to variations in the incoming spectra.

This new method of increasing the spectral resolution from CFA Bayer measurements via demultiplexing allows for a low-cost, low-complex and portable simultaneous multispectral system. We used this system for two applications which were photoplethysmographic imaging and multispectral microscopy.

In the first application we proposed a novel Numerical Spectral Demultiplexing (NSD) method to infer narrow-band spectral information from acquired RGB measurements in order to estimate the heart rate via the computation of motion-compensated skin erythema fluctation analysis. We called this new method NSD Erythema Flucation Analysis (NSDEFA) and compared it against the baseline method of Erythema Flucation Analysis (EFA). We found that we could improve the traditional EFA method by demultiplexing the RGB measurements into 545 nm for the green signal and 640 nm for the red signal. Therefore decomposing the RGB measurements from the camera into narrow-band spectral information can improve the prediction of the heart rate estimation.

In second application we characterized the spectral sensitivity of a Raspberry Pi camera and created a multispectral microscope by demultiplexing the RGB measurements of the camera into a higher spectral signal. We used our multispectral microscope for bright-field multispectral microscopy for botanical specimens as well as for bright-field and dark-field multispectral microscopy for anatomical specimens. Using this numerical spectral demultiplexing microscopy (NSDM) system allowed for a low-cost, portable, point of care system which provided additional information of the different specimens.

Future work consists of using different frameworks, such as neural networks and other machine learning techniques, to improve the numerical demultiplexer. Furthermore, research must be done to improve the accuracy of the forward model since this model is in the most basic form. By incorporating a more comprehensive the forward model, the training data will be more representative of the real world system, and therefore the inverse model will also more more reliable.

References

[1] Rafael C. Gonzalez and Richard E. Woods. *Digital Image Processing (3rd Edition).* Prentice-Hall, Inc., Upper Saddle River, NJ, USA, 2006.

[2] Scott Krig. *Computer Vision Metrics: Survey, Taxonomy, and Analysis.* Apress, 2014.

[3] Algolux. Image processing for next-generation cameras, June 2016.

[4] Lytro. Lytro illum, June 2016.

[5] Bjørn Skovlund Dissing, Olga S. Papadopoulou, Chrysoula Tassou, Bjarne Kjaer Ersbøll, Jens Michael Carstensen, Efstathios Z. Panagou, and George-John Nychas. Using multispectral imaging for spoilage detection of pork meat. *Food and Bioprocess Technology*, 6(9):2268–2279, 2013.

[6] Jonas Franke and Gunter Menz. Multi-temporal wheat disease detection by multi-spectral remote sensing. *Precision Agriculture*, 8(3):161–172, 2007.

[7] S Baronti, A Casini, F Lotti, and S Porcinai. Multispectral imaging system for the mapping of pigments in works of art by use of principal-component analysis. *Applied optics*, 37(8):1299–1309, 1998.

[8] Jose AJ Berni, Pablo J Zarco-Tejada, Lola Suárez, and Elias Fereres. Thermal and narrowband multispectral remote sensing for vegetation monitoring from an unmanned aerial vehicle. *Geoscience and Remote Sensing, IEEE Transactions on*, 47(3):722–738, 2009.

[9] Andrea S Laliberte, Mark A Goforth, Caitriana M Steele, and Albert Rango. Multispectral remote sensing from unmanned aircraft: Image processing workflows and applications for rangeland environments. *Remote Sensing*, 3(11):2529–2551, 2011.

[10] R Calderón, Juan Antonio Navas-Cortés, C Lucena, and Pablo J Zarco-Tejada. High-resolution airborne hyperspectral and thermal imagery for early detection of verticillium wilt of olive using fluorescence, temperature and narrow-band spectral indices. *Remote Sensing of Environment*, 139:231–245, 2013.

[11] MS Kim, YR Chen, PM Mehl, et al. Hyperspectral reflectance and fluorescence imaging system for food quality and safety. *Transactions-American Society of Agricultural Engineers*, 44(3):721–730, 2001.

[12] Renfu Lu and Yankun Peng. Hyperspectral scattering for assessing peach fruit firmness. *Biosystems Engineering*, 93(2):161–171, 2006.

[13] Farnoud Kazemzadeh, Sami Ahmed Haider, Christian Scharfenberger, Alexander Wong, and David A Clausi. Multispectral stereoscopic imaging device: Simultaneous multiview imaging from the visible to the near-infrared. *Instrumentation and Measurement, IEEE Transactions on*, 63(7):1871–1873, 2014.

[14] Yasushi Hiraoka, Takeshi Shimi, and Tokuko Haraguchi. Multispectral imaging fluorescence microscopy for living cells. *Cell structure and function*, 27(5):367–374, 2002.

[15] Mikkel Brydegaard, Zuguang Guan, and Sune Svanberg. Broad-band multispectral microscope for imaging transmission spectroscopy employing an array of light-emitting diodes. *American Journal of Physics*, 77(2):104–110, 2009.

[16] Jason Deglint, Farnoud Kazemzadeh, M. J. Shafiee, Edward Li, Iman Khodadad, Simarjeet S. Saini, Alexander Wong, and D. A. Clausi. Virtual spectral multiplexing for applications in in-situ imaging microscopy of transient phenomena. In *SPIE Optics and Photonics*, August 2015.

[17] Farnoud Kazemzadeh, Chao Jin, Mei Yu, Robert Amelard, Shahid Haider, Simarjeet Saini, Monica Emelko, David A Clausi, and Alexander Wong. Multispectral digital holographic microscopy with applications in water quality assessment. In *SPIE Optical Engineering+ Applications*, pages 957906–957906. International Society for Optics and Photonics, 2015.

[18] Johannes Brauers, Nils Schulte, and Til Aach. Multispectral filter-wheel cameras: Geometric distortion model and compensation algorithms. *Image Processing, IEEE Transactions on*, 17(12):2368–2380, 2008.

[19] Masahiro Yamaguchi, Masanori Mitsui, Yuri Murakami, Hiroyuki Fukuda, Nagaaki Ohyama, and Yasuo Kubota. Multispectral color imaging for dermatology: application

in inflammatory and immunologic diseases. In *Color and Imaging Conference*, volume 2005, pages 52–58. Society for Imaging Science and Technology, 2005.

[20] Neelam Gupta. Acousto-optic-tunable-filter-based spectropolarimetric imagers for medical diagnostic applicationsinstrument design point of view. *Journal of biomedical optics*, 10(5):051802–051802, 2005.

[21] SE Harris and RW Wallace. Acousto-optic tunable filter. *JOSA*, 59(6):744–747, 1969.

[22] Hyunsung Park and Kenneth B Crozier. Multispectral imaging with vertical silicon nanowires. *Scientific reports*, 3, 2013.

[23] Hideaki Haneishi, Takayuki Hasegawa, Asako Hosoi, Yasuaki Yokoyama, Norimichi Tsumura, and Yoichi Miyake. System design for accurately estimating the spectral reflectance of art paintings. *Applied Optics*, 39(35):6621–6632, 2000.

[24] P Stigell, Kimiyoshi Miyata, and Markku Hauta-Kasari. Wiener estimation method in estimating of spectral reflectance from RGB images. *Pattern Recognition and Image Analysis*, 17(2):233–242, 2007.

[25] Izumi Nishidate, Takaaki Maeda, Kyuichi Niizeki, and Yoshihisa Aizu. Estimation of melanin and hemoglobin using spectral reflectance images reconstructed from a digital RGB image by the Wiener estimation method. *Sensors*, 13(6):7902–7915, 2013.

[26] Shuo Chen and Quan Liu. Modified Wiener estimation of diffuse reflectance spectra from RGB values by the synthesis of new colors for tissue measurements. *Journal of Biomedical Optics*, 17(3):0305011–0305013, 2012.

[27] Hui-Liang Shen, Pu-Qing Cai, Si-Jie Shao, and John H Xin. Reflectance reconstruction for multispectral imaging by adaptive wiener estimation. *Optics express*, 15(23):15545–15554, 2007.

[28] Noriyuki Shimano. Recovery of spectral reflectances of objects being imaged without prior knowledge. *Image Processing, IEEE Transactions on*, 15(7):1848–1856, 2006.

[29] Jason Deglint, F. Kazemzadeh, Alexander Wong, and D. A. Clausi. Inference of dense spectral reflectance images from sparse reflectance measurement using non-linear regression modeling. In *SPIE Optics and Photonics*, August 2015.

[30] Jae Hee Song, Choye Kim, and Yangmo Yoo. Vein visualization using a smart phone with multispectral wiener estimation for point-of-care applications. *Biomedical and Health Informatics, IEEE Journal of*, 19(2):773–778, 2015.

[31] Izumi Nishidate, Keiichiro Yoshida, Chiharu Mizushima, Satoko Kawauchi, Shunichi Sato, and Manabu Sato. Multispectral imaging of hemodynamics in exposed brain of rat during cortical spreading depression using wiener estimation method. In *European Conferences on Biomedical Optics*, pages 88040A–88040A. International Society for Optics and Photonics, 2013.

[32] Philipp Urban, Mitchell R Rosen, and Roy S Berns. A spatially adaptive wiener filter for reflectance estimation. In *Color and Imaging Conference*, volume 2008, pages 279–284. Society for Imaging Science and Technology, 2008.

[33] Jon Y Hardeberg. On the spectral dimensionality of object colours. In *Conference on Colour in Graphics, Imaging, and Vision*, volume 2002, pages 480–485. Society for Imaging Science and Technology, 2002.

[34] Z. Sadeghipoor, Y.M. Lu, and S. Süsstrunk. Optimal spectral sensitivity functions for single sensor color imaging. In *Proc. SPIE Conference on Digital Photography VIII*, Burlingame, Jan. 2012.

[35] B.E. Bayer. Color imaging array, July 20 1976. US Patent 3,971,065.

[36] Leo Breiman. Random Forests. *Machine Learning*, 45(1):5–32, 2001.

[37] Alexei A Kamshilin, Serguei Miridonov, Victor Teplov, Riku Saarenheimo, and Ervin Nippolainen. Photoplethysmographic imaging of high spatial resolution. *Biomedical optics express*, 2(4):996–1006, 2011.

[38] Yu Sun, Charlotte Papin, Vicente Azorin-Peris, Roy Kalawsky, Stephen Greenwald, and Sijung Hu. Use of ambient light in remote photoplethysmographic systems: comparison between a high-performance camera and a low-cost webcam. *Journal of Biomedical Optics*, 17(3):037005–1–037005–10, 2012.

[39] Dangdang Shao, Yuting Yang, Chenbin Liu, Francis Tsow, Hui Yu, and Nongjian Tao. Noncontact monitoring breathing pattern, exhalation flow rate and pulse transit time. *IEEE Transactions on Biomedical Engineering*, 61(11):2760–2767, 2014.

[40] Mayank Kumar, Ashok Veeraraghavan, and Ashutosh Sabharval. Distanceppg: Robust non-contact vital signs monitoring using a camera. *Biomedical Optics Express*, 6(5):1565–1588, 2015.

[41] Lingqin Kong, Yuejin Zhao, Liquan Dong, Yiyun Jian, Xiaoli Jin, Bing Li, Yun Feng, Ming Liu, Xiaohua Liu, and Hong Wu. Non-contact detection of oxygen saturation based on visible light imaging device using ambient light. *Optics Express*, 21(15):17464–17471, 2013.

[42] Ming-Zher Poh, Daniel J McDuff, and Rosalind W Picard. Non-contact, automated cardiac pulse measurements using video imaging and blind source separation. *Optics Express*, 18(10):10762–10774, 2010.

[43] Shuchang Xu, Lingyun Sun, and Gustavo Kunde Rohde. Robust efficient estimation of heart rate pulse from video. *Biomedical Optics Express*, 5(4):1124–1135, 2014.

[44] Daniel McDuff, Sarah Gontarek, and Rosalind W Picard. Improvements in remote cardiopulmonary measurement using a five band digital camera. *Biomedical Engineering, IEEE Transactions on*, 61(10):2593–2601, 2014.

[45] Audrey Chung, Xiao Yu Wang, Robert Amelard, Christian Scharfenberger, Joanne Leong, Jan Kulinski, Alexander Wong, and David A Clausi. High-resolution motion-compensated imaging photoplethysmography for remote heart rate monitoring. In *SPIE BiOS*, pages 93160A–93160A. International Society for Optics and Photonics, 2015.

[46] Carlo Tomasi and Takeo Kanade. *Detection and tracking of point features*. School of Computer Science, Carnegie Mellon Univ. Pittsburgh, 1991.

[47] Paul Viola and Michael Jones. Rapid object detection using a boosted cascade of simple features. In *Computer Vision and Pattern Recognition, 2001. CVPR 2001. Proceedings of the 2001 IEEE Computer Society Conference on*, volume 1, pages I–511. IEEE, 2001.

[48] Richard Y Ha, Kimihiro Nojima, William P Adams Jr, and Spencer A Brown. Analysis of facial skin thickness: defining the relative thickness index. *Plastic and reconstructive surgery*, 115(6):1769–1773, 2005.

[49] Hao Gong and Michel Desvignes. Hemoglobin and melanin quantification on skin images. In Aurlio Campilho and Mohamed Kamel, editors, *Image Analysis and Recognition*, volume 7325 of *Lecture Notes in Computer Science*, pages 198–205. Springer, 2012.

[50] American Heart Association. Target Heart Rates. http://www.heart.org/. (22 March 2013).

[51] ME Dickinson, G Bearman, S Tille, R Lansford, and SE Fraser. Multi-spectral imaging and linear unmixing add a whole new dimension to laser scanning fluorescence microscopy. *Biotechniques*, (31):1272–1274, 2002.

[52] Richard M Levenson, David T Lynch, Hisataka Kobayashi, Joseph M Backer, and Marina V Backer. Multiplexing with multispectral imaging: from mice to microscopy. *ILAR journal*, 49(1):78–88, 2008.

[53] Michael C Adams, Wendy C Salmon, Stephanie L Gupton, Christopher S Cohan, Torsten Wittmann, Natalie Prigozhina, and Clare M Waterman-Storer. A high-speed multispectral spinning-disk confocal microscope system for fluorescent speckle microscopy of living cells. *Methods*, 29(1):29–41, 2003.

[54] Mikkel Brydegaard, Aboma Merdasa, Hiran Jayaweera, Jens Ålebring, and Sune Svanberg. Versatile multispectral microscope based on light emitting diodes. *Review of Scientific Instruments*, 82(12):123106, 2011.

[55] NL Everdell, IB Styles, E Claridge, JC Hebden, and AS Calcagni. Multispectral imaging of the ocular fundus using led illumination. In *European Conferences on Biomedical Optics*, pages 73711C–73711C. International Society for Optics and Photonics, 2009.

[56] Joni Orava, Jussi Parkkinen, Markku Hauta-Kasari, Paula Hyvönen, and Atte von Wright. Temporal clustering of minced meat by RGB-and spectral imaging. *Journal of Food Engineering*, 112(1):112–116, 2012.

[57] Izumi Nishidate, Keiichiro Yoshida, Satoko Kawauchi, Shunichi Sato, and Manabu Sato. In vivo imaging of scattering and absorption properties of exposed brain using a digital red-green-blue camera. In *SPIE BiOS*, pages 89280N–89280N. International Society for Optics and Photonics, 2014.